Tunneling and Origin of Large Access Resistance in Layered-Crystal Organic Transistors

Takamasa Hamai, Shunto Arai, Hiromi Minemawari, Satoru Inoue, Reiji Kumai, and Tatsuo Hasegawa

Phys. Rev. Applied **8**, 054011 — Published 7 November 2017

DOI: 10.1103/PhysRevApplied.8.054011

Tunneling and origin of large access resistance in layered-crystalline organic transistors

Takamasa Hamai*, Shunto Arai, Hiromi Minemawari, Satoru Inoue, Reiji Kumai, and Tatsuo Hasegawa

T. Hamai, Dr. S. Arai, Prof. T. Hasegawa

Department of Applied Physics, The University of Tokyo, Tokyo 113-8656, Japan

E-mail: hamai@hsgw.t.u-tokyo.ac.jp

Dr. H. Minemawari, Dr. S. Inoue, Prof. T. Hasegawa

National Institute of Advanced Industrial Science and Technology (AIST), Tsukuba 305-8565, Japan

Prof. R. Kumai

Condensed Matter Research Center (CMRC) and Photon Factory, Institute of Materials Structure Science, High Energy Accelerator Research Organization (KEK), Tsukuba 305-0801, Japan

Abstract

Layered crystallinity of organic semiconductors is crucial to obtain high-performance organic thin-film transistors (OTFTs), as it allows both smooth channel/gate-insulator interface formation and efficient two-dimensional carrier transport along the interface. However, the role of vertical transport across the crystalline molecular layers in device operations has not been a crucial subject so far. Here we show that the interlayer carrier transport causes unusual nonlinear current–voltage characteristics and enormous access resistance in extremely high-quality single-crystalline OTFTs based on Ph-BTBT-C_{10} that involve inherent multiple semiconducting π-conjugated layers interposed respectively by electrically-inert alkyl-chain layers. The output characteristics present layer-number (n)-dependent nonlinearity that becomes more evident at larger n ($1 \leq n \leq 15$), demonstrating tunnelling across multiple alkyl-chain layers. The n-dependent device mobility and four-probe measurements reveal that the alkyl-chain layers generate a large access resistance that suppresses the device mobility from the intrinsic value of about 20 cm^2/Vs. Our findings clarify the reason why device characteristics are distributed in single-crystalline OTFTs. (157 words)

I. Introduction

High layered crystallinity is regarded as the most fundamental requirement for organic semiconductors (OSCs) in obtaining high-performance organic thin-film transistors (OTFTs). Studies over the last decade have revealed that all the small-molecule OSCs giving high-performance OTFTs exhibit high layered crystallinity, which is associated mostly with the formation of the *layered-herringbone* (LHB)-type molecular packing motif[1–8]. The LHB is known to be the most suitable packing motif for producing two-dimensional molecular assemblies composed of aligned planar-like π-electron molecules. Thus, the obtained high layered crystallinity allows the production of uniform channel semiconductor layers that have flat semiconductor–insulator interfaces, along which efficient charge carrier transport takes place[2,3,9–12].

Among the wide variety of these materials developed so far, it was recently reported that in some OSC materials the layered crystallinity is considerably enhanced by substituting the π-electron cores asymmetrically with normal alkyl chains[6,8,10]. A particular example is seen in benzothieno[3,2-*b*][1]benzothiophenes (BTBT) with asymmetric phenyl and alkyl-chain substitutions (Ph-BTBT-C_m): when the BTBT core is substituted by sufficiently long alkyl chains ($m \geq 5$), the compounds exhibit bilayer-type LHB packing whose bilayer unit is formed by the antiparallel alignment of a pair of polar monomolecular layers, each composed of unipolar orientations of asymmetric molecules, such that the π-electron cores are in contact[4,6]. It was demonstrated that the high layered crystallinity in Ph-BTBT-C_m can be ascribed to the separate formation of semiconducting π-electron-core layers and subsidiary alkyl-chain layers, where the intralayer chain–chain interactions contribute to stabilize the layered molecular packing of the π-electron-core layers[6]. Note that the alkyl-chain substitution of OSCs was originally introduced to enhance the solvent solubility for use in solution-based thin-film processing[13,14], which now attracts considerable attention for the expectation of realizing printing-based device production (or printed electronics) technologies. In this context, these materials are quite promising, because the resultant high layered crystallinity allows the formation of extremely uniform, large-area thin films through the self-organization of molecules under rather mild conditions within the OSC solution[2,3,6,8].

It is expected in such layered crystals that the carrier transport becomes highly anisotropic in nature, because the intermolecular interactions within and across the molecular layers are considerably different to each other. In particular, anisotropic conduction should become more apparent in the alkyl-substituted OSCs because the electrically inert alkyl-chain layers should separate the carrier transport between, along, and across the semiconducting π-conjugated layers[15]. However, such anisotropic conduction in the layered crystals and thus its role in device operations have not yet been understood.

In this study, we investigated the inherent anisotropic carrier transport in 2-decyl-7-phenyl[1]-BTBT (Ph-BTBT-C_{10}) OTFTs composed of nearly perfect single-crystalline thin films with both controllability and uniformity of the molecular-level thickness over the whole channel region. For this purpose, we fabricated Ph-BTBT-C_{10} single-crystalline thin films that have a controllable layer-number thickness of between 1 and 15 over a millimeter-scale area by a controlled solution process for self-organized single-crystalline ultrathin film formation. Bottom-gate, top-contact field-effect transistor characteristics of the films were investigated using two- and four-probe techniques[16–19]. As a result, we succeeded in separately measuring the contributions of the intralayer and the interlayer carrier transport in the single-crystalline OTFTs. Based on the results, we discuss how the active layer thickness affects the device performance in single-crystalline Ph-BTBT-C_{10} OTFTs.

II. Experiment

Ph-BTBT-C_{10} was synthesized and purified as described elsewhere[6]. We used heavily *p*-doped silicon wafer with (or without) 100 nm thermally-grown silica layer as substrates. They were fully cleaned by sonication for 3 min in each of de-ionized water, acetone, ethanol, and de-ionized water. We used a blade coating technique at regulated temperatures to fabricate large-area single-crystalline thin films of Ph-BTBT-C_{10} with use of the solution in chlorobenzene. We used a thin glass plate coated with Cytop (CTL-809M Asahi Glass Co., Ltd., Japan) as the coating blade whose motion is controlled by a stepping motor (SHOT-302GS; SIGMA KOKI Co., Ltd., Japan). The thickness of the single-crystalline films could be roughly controlled by the solution concentration and sweep rate, ranged from 0.1 to 0.15 wt% and from 1 to 3 μm/s, respectively.

The obtained single-crystalline thin films were characterized by polarized optical microscope (Axio Scope A1;

Carl Zeiss Microscopy GmbH, Germany). Thickness and height profiles of the films were measured by tapping-mode AFM (Dimension 3000 Nanoscope IIIa; Bruker Co., Ltd., USA). The X-ray diffraction data were collected by an imaging plate diffractometer (DSC; Rigaku Co., Ltd., Japan) at BL-8B (λ = 1.0 Å) in Photon Factory (PF), High-Energy Accelerator Research Organization (KEK) for the results shown in Fig. 5(c), and by thin-film diffractometer (SOR-SmartLab; Rigaku Co., Ltd., Japan) at BL-7C (λ = 1.38 Å) for the results shown in Fig. 5(d). The diffraction intensity was recorded by an oscillation photograph ($\Delta\omega = 5^{\circ}$) in the former and by a ω-2θ scan using scintillation counter in the latter.

To fabricate single-crystalline OTFTs with bottom-gate top-contact geometry, source and drain electrodes were fabricated by thermal deposition of Au through a shadow mask. We took much care to suppress thermal radiation from the evaporation source to the semiconductor films, by putting radiation shield over the hot metal source. The shield has a small hole with a diameter of 5 mm, through which the evaporated Au and heat radiation can pass. We also controlled the substrate temperature at 20 °C by a circulation cooling. For the proper evaluation of the mobility, part of thin films outside the channel was trimmed away by using micromanipulator (Axis-Pro; Systems Engineering Inc., Japan). The OTFT characteristics were measured by one or a pair of two-channel source/measurement units (B2912A; Keysight Technologies, Co., Ltd., USA) for the conventional two-probe and gated-four-probe measurements, respectively. In the measurement of transfer characteristics in linear regime (Fig. 6(a-c)), applied drain voltage was not unified for the films with different layer-number thickness, because of the different injection voltage.

III. Results and discussion

A. Layer-number control of single-crystalline thin films

Large-area single-crystalline domains of Ph-BTBT-C_{10} with controlled layer-number (n) thicknesses between n = 1 (5.3 nm) and n = 15 (80 nm) were successfully grown by adjusting processing parameters of a blade-coating technique (Fig. 1(a)). Fig. 1(b) shows an example of obtained single-crystalline thin film after the whole film other than this single-crystalline domain was trimmed out. The obtained films are composed of large single-crystalline domains, each of which exhibits a clear change in brightness on rotating the film about an axis perpendicular to the substrate in the crossed-Nicol polarized microscope image (Figs. 1(c, d)). Each of the single-crystalline domains is composed of several distinct regions with different colors (Fig. 2(a)). The mono-colored area corresponds to film with a constant layer-number thickness, as confirmed by atomic force microscopy (AFM) and X-ray diffraction measurements, and also by the color analyses for multilayer films, as described below.

We conducted AFM measurements over the entire film area, and the mono-colored area was observed to have a constant height. In contrast, the images showed clear molecular steps at the boundaries between different colored areas. An example is given in Fig. 2(b): No steps were observed in the AFM height profiles of the ocher-colored or light-blue-colored areas, but the height profile at the border exhibits multiple steps with a step height of 5.3 nm that corresponds to the bilayer thickness. We did not observe step heights other than 5.3 nm on the Ph-BTBT-C_{10} single-crystalline films, which is in contrast to the different step heights seen on spin-coated polycrystalline thin films of Ph-BTBT-C_{10} produced at an elevated temperature[10].

We measured out-of-plane X-ray diffraction from the mono-colored area of the films (Fig. 3(a)). To detect the diffraction from this area only, we removed the film around the mono-colored area; an example is presented in Fig. 3(b). We observed clear Laue fringes in addition to the (00l) Bragg peaks, as presented in the diffractograms shown in Figs. 3(c, d). The observed Laue fringes are coincident with the respective layer-number thickness as measured by AFM. Note that this is a unique example for the observation of clear Laue fringes for organic single-crystalline thin films[20–25]. These observations afford clear evidence that the films have well-defined layer structure of an exceptionally homogeneous molecular-level thickness over the whole mono-colored area. The agreement of the layer numbers in the AFM profiles and the Laue fringes ensures the accuracy of the discrete layer-number determination by AFM. We hereafter use the term "layer number", n, to refer to the number of bilayer units which are stacked to form the thin films on the substrate, and we analysed the thickness dependence of the device characteristics by using the layer number measured with AFM as a key parameter.

It is important to point out that the layer-number thickness can be easily discriminated by the color of the films. The areas surrounded by red lines in Figs. 4(a-d) are single-crystalline and molecularly flat domains, whose thickness was confirmed to be 1 (Fig. 4(a)), 5 (Fig. 4(b)), 10 (Fig. 4(c)), 14 (Fig. 4(d)) bilayer thickness by AFM measurement. These films show

clear difference of color, blue for ultrathin film and light-blue or cream for thicker films, as seen in Fig. 2(a). This indicates that the difference of thickness causes distinguishable change of reflectivity and allows us to conduct both two- and four-probe measurements of single-crystalline films with variable layer-number thicknesses ($1 \le n \le 15$). To understand the origin of the color change, we conducted color analyses by simulating the reflectivity of the multilayer films, *i.e.*, Ph-BTBT-C_{10} (5.3 × n nm)/SiO_2 (100 nm)/Si (0.6 mm) (see Fig. 5(a)), based on Fresnel's equation.

At each interface (j=1, 2, 3), reflectivity for vertically incident light with wavelength λ can be obtained by the well-known formula $r_j(\lambda) = \frac{n_{j+1}(\lambda)-n_j(\lambda)}{n_{j+1}(\lambda)+n_j(\lambda)}$, where $n_j(\lambda)$ is the real part of refractive index of the layer j. For $j \ge 2$, we should consider the multiple reflection to obtain Fresnel's coefficient ρ_j

$$\rho_j = \frac{r_j+\rho_{j-1}\exp[-4\pi i(n_j-i\kappa_j)d_j/\lambda]}{1+r_j\rho_{j-1}\exp[-4\pi i(n_j-i\kappa_j)d_j/\lambda]} \quad (1)$$

where κ_j, d_j denote the imaginary part of reflective index and thickness of layer j, respectively. By substituting $\rho_1 = r_1$ and calculating ρ_j until j=3, we obtained the reflection spectrum $R(\lambda) = |\rho_3(\lambda)|^2$. We used $n_2 = 1.8$ and $\kappa_2 = 0$ for Ph-BTBT-C10 layer and the reflactive indices of Si and SiO2 were obtained elsewhere[26,27]. Fig. 5(b) shows the reflectivity of R (λ=700 nm), G (λ=550 nm), and B (λ=440 nm) for $1 \le n \le 20$, which agreed well with the experimental color of single-crystalline thin films (Figs. 4(a-d)).

B. Layer-number-dependent injection voltage

We produced OTFT devices whose channels are composed of single-crystalline domains with a constant layer-number thickness. The channel dimensions of all the devices were 400 μm (width) × 250 μm (length) for both the two- and four-probe measurements. Source and drain electrodes were fabricated with care to suppress thermal damage of the semiconductor films, and we found that neither the Au penetration into the single-crystalline films nor the thermal damage by the Au deposition did not take place, considering the layer-number-dependent device characteristics and access resistance, as presented below. The area of constant layer-number thickness also extends over the principal area under the source and drain electrodes for carrier injection. We first conducted measurements of the transfer and output characteristics using a conventional two-probe technique (i.e., V_d and I_d are probed by the source and drain electrodes).

Notable layer-number dependence was observed in the output characteristics, as presented in Figs. 6(a–c). Nearly ohmic features are observed in the ultrathin film (n = 2), whereas the output curve becomes fairly nonlinear in the low-voltage range in thicker films (n = 6 and 15). The origin of the nonlinearity should not be ascribed to Schottky barriers at the metal–semiconductor interface[28–31], considering the absence of nonlinearity in the n = 2 film and also the increased nonlinearity in the thicker films as summarized in Fig. 7(a). Rather, carrier injection should be inhibited by the much larger interlayer access resistance in the low-V_d range.

To elucidate the n-dependent nonlinearity, we estimated the injection voltage (V_{inj}) to be the voltage at the point where the extrapolated linear fit of the I_d–V_d curve (at V_g = − 40 V) crosses the V_d axis (see Figs. 6(a–c)). The fitting was performed around the point with the highest slope ranged 5 V. Note that the values correspond to the required drain bias for injecting carriers into the channels. We see that V_{inj} reaches a maximum of about −10 V for the n = 15 film. Note that in top-contact OTFTs based on polycrystalline Ph-BTBT-C_{10} films ohmic features were observed in the output characteristics even in the case of films with a thickness of 35 nm, which corresponds to the n = 7 film in this study[10]. This implies that the highly ordered alkyl-chain layers should be responsible for the notable nonlinearity in the output characteristics. The V_{inj} plot, shown in Fig. 7(b), can be well fitted by a linear dependence on n − 1, corresponding to the number of paired alkyl-chain layers, in the following form:

$$V_{inj} = (n\text{-}1)\times 0.67 \text{ V} \quad (2)$$

Here, we ignored the contribution by the unpaired alkyl-chain layer on the top film surface. It is most probable that the observed feature of the V_{inj} is ascribable to the tunneling of carriers across the paired alkyl-chain layers, as discussed in the next subsections.

C. Layer-number-dependent device mobility and access resistance

Typical transfer characteristics in the linear regime (V_d = − 15 V) are presented in Figs. 6(a-c) for devices with different layer numbers of n = 2, 6, and 15. The device mobility (μ_{dev}^n) in the linear regime is estimated by the standard equation;

$$I_d = (W/L)\mu_{dev}^n C_i(V_g - V_{th})V_d \quad (3)$$

The device mobility is highest in the n = 2 film (μ_{dev}^2 = 17.5 $cm^2V^{-1}s^{-1}$) and lower in the thicker films (μ_{dev}^6 = 4.3 $cm^2V^{-1}s^{-1}$ and μ_{dev}^{15} = 3.5 $cm^2V^{-1}s^{-1}$). Fig. 7(c) summarizes the n dependence of μ_{dev}^n for all the measured devices (63 in total).

The average value of μ_{dev}^{n} decreases with an increase in n.

To extract the components of the interlayer transport, we can describe μ_{dev}^{n} in terms of the channel resistance R_{ch}, interface resistance R_{int}, and interlayer access resistance R_{acc}^{n} by using the following equation:

$$\mu_{dev}^{n} \propto 1/(R_{ch}+R_{int}+R_{acc}^{n}) \quad (4)$$

Here, we assume that R_{acc}^{n} is the only parameter that contributes to the n dependence of μ_{dev}^{n} (see Fig. 7(d)) and R_{acc}^{n} can be divided into the contribution from both source electrode ($R_{acc,S}$) and drain electrode ($R_{acc,D}$); $R_{acc}^{n} = R_{acc,S}^{n} + R_{acc,D}^{n}$. We then define the mobility attenuation factor[32], $\theta(n)$, as

$$\theta(n) = R_{acc}^{n}/(R_{ch}+R_{int}) \quad (5)$$

$$\mu_{dev}^{n} = \mu_{dev}^{1}/(1+\theta(n)). \quad (6)$$

Here, $\theta(n)$ denotes the ratio of R_{acc}^{n} to the total resistance of the single-bilayer device (n = 1), and we assume that the contribution by the unpaired alkyl-chain layer on the top film surface can be ignored for all the devices. We also consider that the parasitic resistance (R_p) only comes from the access resistance, $R_p \approx R_{acc}$, in contrast to the previous report[28]. Here we did not use the term "contact resistance", as we would like to mention that not only the electrode/semiconductor interface but also the vertical transport within semiconductor layer considerably affects the OTFT characteristics. We found that the experimental results are well reproduced by equation (6) when $\theta(n)$ takes the form

$$\theta(n) = (n\text{-}1) \times 0.47. \quad (7)$$

The fit, assuming μ_{dev}^{1} = 18.5 $cm^2V^{-1}s^{-1}$, is shown in Fig. 7(c) by the solid curve. It is clear that the interlayer access resistance is proportional to $n - 1$, although the experimental value of μ_{dev}^{1} shows a large deviation from this trend. The decreased mobility for single monolayer device was reported experimentally[33] and was discussed by calculation[34] in terms of the enhanced effect of Coulomb scattering and energetic disorder. However, we consider that the origin to suppress the mobility as observed in Fig. 7(c) should be different because of the higher layered-crystalline nature of the film.

D. Gated-four-probe measurements

Gated-four-probe technique (Fig. 8(a)) is used to further investigate the contribution of interlayer- and intralayer conduction. Typical four-probe transfer characteristics in the linear regime are presented in Fig. 8(b). The calculated parasitic resistance at source and drain electrodes (R_s, R_d) were also plotted in the inset of Fig. 8(b). Both the values of R_s and R_d are comparable to the value of R_{ch}, indicating that the access resistances at both source and drain electrodes affect the device characteristics. Note that in the experimental estimation of R_s and R_d, we extrapolated potential gradient between two sense electrodes to source and drain electrode to obtain potential drop between the electrode and the channel layer. Then, the R_s and R_d was obtained by dividing the potential drops by I_d. However, it is also known that the potential along the channel layer does not change linearly, which was previously confirmed by Kelvin probe microscopy measurements.[35,36] According to the reports, the resistance along the channel close to the drain electrode should be larger than that close to the source electrode. However, this effect is not included in our estimation based on the gradual channel approximation. Hence, such a difference of local channel resistance should be included in the values of R_s and R_d. We consider that this should be the reason why R_d is higher than R_s. In contrast, $R_{acc,S}$ and $R_{acc,D}$ (shown in Fig. 7d) should be basically same, because these are connected in series with each other.

The V_g dependence of the field-effect mobility estimated by the slopes of the transfer curves are shown in Fig. 8(c) for both the two-probe (μ_{dev}^{n}) and gated-four-probe measurements (μ_{gFPP}) for the n = 2 film. The μ_{gFPP} in this measurement is estimated as 21.6 $cm^2V^{-1}s^{-1}$, which is about two times larger than μ_{dev}^{2}. The results clearly demonstrates the effect of a large access resistance.

Fig. 8(d) summarizes the layer-number dependence of μ_{gFPP} for all the measurements. For $2 \leq n \leq 4$, μ_{gFPP} presents slightly higher values as compared to the value estimated by the n-dependent two-probe measurements (18.5 $cm^2V^{-1}s^{-1}$). In contrast, μ_{gFPP} presents a much lower value at n = 1 and a much higher value at n = 5. The results indicate that the channel mobility should be dependent on the layer number n, though we assumed in Eq. (4) that the intrinsic mobility is invariant against an increase in n. Furthermore, μ_{gFPP} becomes much lower again at $n \geq 6$. We conjecture that it might be quite difficult to measure the correct electrical potential within the channel layer that is located at the semiconductor/insulator interface for thicker films, as the sense electrodes are located on the top surfaces of the thick semiconductor layers. (The sense electrodes were thermally deposited onto semiconductor thin films at the same time as source/drain electrodes were fabricated. It means that the large access resistance should also exist between sense electrode and channel layer.) Additionally, the sense electrodes were controlled to flow no current by the use of source measure units, which causes extremely larger

access resistance between sense electrode and channel layer than that between source/drain electrode and channel layer. Hence, the extremely large access resistance may cause incorrect estimation of electrical potential within the channel layer for thicker films. The decrease of error bar should be due to the decrease of the average mobility. The standard deviation over the average mobility is fluctuating around 0.5 for all n.

E. Discussion

The effect of the parasitic resistance between the channels and electrodes has been one of the most important issues in the development of OTFTs. The present study demonstrates that well-aligned molecules may maximize the large access resistance between the electrode and channel, although there are ideally no grain boundaries in the single-crystalline thin films that can minimize the channel resistance.

The interlayer access resistance per one bilayer ($R_{1\text{bilayer}}$) can be estimated to be as large as $R_{1\text{bilayer}}$ = 389–472 Ωcm (Tab. 2) in the Ph-BTBT-C_{10} single-crystalline thin films by the fitting of device mobility with equation (6) and by gated-four-probe measurement, respectively. In sharp contrast, previous reports showed that the estimated active-layer thickness dependence of the mobility and parasitic resistance is very small in polycrystalline thin films. The parasitic access resistance was estimated as $R_{5.3\text{nm}}$ = 80 Ωcm (5.3 nm is the single bilayer thickness) for spin-coated polycrystalline thin films of Ph-BTBT-C_{10} produced at an elevated temperature[10]. This small access resistance might be due to the different nature of the polycrystalline thin films that are composed of several parts where the well-defined insulating alkyl-chain structure is violated along the perpendicular to the layer plane so that a current path can exist without crossing the insulating alkyl-chain layer.

The large access resistance in single-crystalline thin film should be an important issue, particular for short channel devices. Even our devices with L=250 μm exhibited notable effect from access resistance. The parasitic effect will be enhanced in short channel devices, where R_p dominates the device operation due to small R_{ch}: The device mobility will show much smaller value than that obtained with long channel devices described above. Therefore, the access resistance from alkyl insulating layer should disturb us from fabricating small-size and fast-operating single-crystalline OTFTs.

All the experimental results demonstrate that Ph-BTBT-C_{10} single-crystalline thin films exhibit highly anisotropic carrier transport and nonlinear current–voltage characteristics along a direction perpendicular to the film plane. It is most probable that the observed nonlinearity should be ascribed to tunneling across the electrically inert alkyl-chain layers[37–43]. Tunneling across the insulating alkyl-chain layer has previously been discussed for self-assembled monolayers (SAM) that are chemically bonded on metal electrodes[38–43]. The nonlinear features as observed in an SAM device are quite similar to our observations. It is clear that the linear dependence of V_{inj} and $R_{acc}{}^{n}$ on n–1 is due to the multiple tunnel barriers that are connected in series by the interposed semiconducting layers between the channel and electrode. We used Simmons equation for describing the tunneling resistance[37],

$$I_{\text{tunnel}} = \frac{e}{4\pi h d^2} S \left\{ \left(\phi_0 - \frac{eV}{2}\right) \exp\left[-\frac{4\pi d}{h} (2m^*)^{\frac{1}{2}} \left(\phi_0 - \frac{eV}{2}\right)^{\frac{1}{2}} \right] - \left(\phi_0 + \frac{eV}{2}\right) \exp\left[-\frac{4\pi d}{h} (2m^*)^{\frac{1}{2}} \left(\phi_0 + \frac{eV}{2}\right)^{\frac{1}{2}} \right] \right\},$$

where □$_0$, m^*, d, and S denote effective mass, barrier height and barrier width of tunneling barrier, and effective area for carrier injection, respectively. The dashed curves in Fig. 7a are simulated I_d–V_d curves obtained by solving Kirchhoff equation $I_{\text{tunnel}} = I_{\text{FET}}$[38,39,44].

We have assumed a tunnel barrier height of ϕ_0 = 1.0 eV, an effective mass $m^* = m_e$ (which are consistent with previous reports[38–41]), and a symmetric band structure for both sides of the tunnel barrier, assuming that both sides are composed of π-conjugated BTBT layers that have sufficient conductivity. The calculated result exhibits similar exponential-like behaviour to the experimental results, where the tunnel resistance monotonically decreases with an increase in voltage. We note that R_{acc} linearly increases with the layer number, which excludes the possibility that space-charge-limited current (SCLC) dominates the interlayer transport.

The effect of the insulating alkyl-chain layers was also discussed in regards to the results of Kelvin force microscope (KFM) measurements on layered crystalline *di*C_8-BTBT film[15]. In contrast, the present study clearly demonstrates that the insulating alkyl-chain layer in the highly layered crystalline OSCs plays crucial roles in the OTFT device operations in terms of the tunneling and concomitant large parasitic access resistance.

Finally, it might be important to mention that hole injection from the source electrodes (and hole ejection to the drain electrodes) should have large spatial distribution over the electrode–semiconductor interfaces when R_{acc} is large. This is in contrast to the conventional OTFTs whose carrier injection

should occur at around the closest edge of the electrodes to the channels[45]. To confirm the effect on the tunneling-based access resistance in realistic devices, we numerically estimated the ratio of carrier injection from the single thicker domain 1 and the outside thinner domain 2, as presented in Fig. 9. The ratio was estimated by comparing the channel conductance and vertical tunneling conductance at each domains. We assumed r_{ch}=402 Ω/μm (assuming μ=20 cm^2/Vs, V_g=10, W=400 μm) as channel resistance per length, and also . We assumed that carrier injection mainly takes place over the near-edge area (right side of the broken line in Fig. 9(a)) to define $r_{acc} = (n\text{-}1)\, r_{1bilayer} = 10^4\ (n\text{-}1)$ Ω for 400x50 μm^2 area. The spatial distribution of channel voltage below the electrode (V_{ch} (x), see Fig. 9(b)) and vertical current density ($J_{\perp}(x)$) was introduced by calculating transfer length[45]. Based on these estimations, we used devices in which more than 80 % of carrier injection was occurred in the domain 1 in this paper.

IV. Conclusions

We fabricated single-crystalline thin film of Ph-BTBT-C10 with large area more than 1 mm^2 and controllable layer-number thickness ($1 \leq n \leq 15$) by blade coating. The fabricated thin films showed clear Laue fringes, which indicates highly homogeneous layered structure. Single-crystalline thin film transistor with bottom-gate top-contact geometry exhibited notable layer-number dependence in nonlinear carrier injection and device mobility. The analysis on layer-number dependence and simulation of nonlinear carrier injection revealed that material's substituted alkyl chain aggregated to form alkyl insulating layers, which caused tunnelling-like transport in interlayer conduction and hence large nonlinear interlayer access resistance. The significance of access resistance was also confirmed by large difference between four-probe mobility and device mobility and decrease of four-probe mobility in large n. We consider that an uncontrolled film thickness and concomitant enormous access resistance as demonstrated in this study should be the main reasons for the large distribution of single-crystalline OTFT device characteristics that have been reported so far[2,3,46]. We suggest that, notwithstanding these disadvantages, the intrinsic alkyl-chain layers, as demonstrated in this study, might also lead to a new paradigm for the single-crystalline OTFTs, if the barrier characteristics are better utilized. For example, we might be able to realize ultralow voltage OTFT operation, if the alkyl-chain layers function as built-in gate dielectric layers that have extremely homogeneous and ultrathin characteristics.

Acknowledgments

We are grateful to Nippon Kayaku Co., Ltd., for providing BTBT. The X-ray measurement was performed with the approval of the Photon Factory Program Advisory Committee (no. 2014S2-001). This work was supported by the Japan Society for the Promotion of Science (JSPS) KAKENHI Grant 26246014 and the Japan Science and Technology Agency (JST) through the Strategic Promotion of the Innovative Research and Development Program (S-Innovation).

References

[1] H. Iino and J. Hanna, Liquid crystalline thin films as a precursor for polycrystalline thin films aimed at field effect transistors. J. Appl. Phys. **109**, 74505 (2011).

[2] H. Minemawari, T. Yamada, H. Matsui, J. Tsutsumi, S. Haas, R. Chiba, R. Kumai, and T. Hasegawa, Inkjet printing of single-crystal films. Nature **475**, 364 (2011).

[3] C. Mitsui, T. Okamoto, M. Yamagishi, J. Tsurumi, K. Yoshimoto, K. Nakahara, J. Soeda, Y. Hirose, H. Sato, A. Yamano, T. Uemura, and J. Takeya, High-performance solution-processable N-shaped organic semiconducting materials with stabilized crystal phase. Adv. Mater. **26**, 4546 (2014).

[4] H. Minemawari, J. Tsutsumi, S. Inoue, T. Yamada, R. Kumai, and T. Hasegawa, Crystal structure of asymmetric organic semiconductor 7-decyl-2-phenyl[1]benzothieno[3,2-b][1]benzothiophene. Appl. Phys. Express **7**, 91601 (2014).

[5] G. Schweicher, V. Lemaur, C. Niebel, C. Ruzié, Y. Diao, O. Goto, W.-Y. Lee, Y. Kim, J.-B. Arlin, J. Karpinska, A.R. Kennedy, S.R. Parkin, Y. Olivier, S.C.B. Mannsfeld, J. Cornil, Y.H. Geerts, and Z. Bao, Bulky End-Capped [1]Benzothieno[3,2- b]benzothiophenes: Reaching High-Mobility Organic Semiconductors by Fine Tuning of the Crystalline Solid-State Order. Adv. Mater. **27**, 3066 (2015).

[6] S. Inoue, H. Minemawari, J. Tsutsumi, M. Chikamatsu, T. Yamada, S. Horiuchi, M. Tanaka, R. Kumai, M. Yoneya, and T. Hasegawa, Effects of Substituted Alkyl Chain Length on Solution-Processable Layered Organic Semiconductor Crystals.

Chem. Mater. **27**, 3809 (2015).

[7] K. Miyata, S. Tanaka, Y. Ishino, K. Watanabe, T. Uemura, J. Takeya, T. Sugimoto, and Y. Matsumoto, Microscopic hole-transfer efficiency in organic thin-film transistors studied with charge-modulation spectroscopy. Phys. Rev. B **91**, 195306 (2015).

[8] H. Minemawari, M. Tanaka, S. Tsuzuki, S. Inoue, T. Yamada, R. Kumai, Y. Shimoi, and T. Hasegawa, Enhanced Layered-Herringbone Packing due to Long Alkyl Chain Substitution in Solution-Processable Organic Semiconductors. Chem. Mater. **29**, 1245 (2017).

[9] Y. Yuan, G. Giri, A.L. Ayzner, A.P. Zoombelt, S.C.B. Mannsfeld, J. Chen, D. Nordlund, M.F. Toney, J. Huang, and Z. Bao, Ultra-high mobility transparent organic thin film transistors grown by an off-centre spin-coating method. Nat. Commun. **5**, 3005 (2014).

[10] H. Iino, T. Usui, and J. Hanna, Liquid crystals for organic thin-film transistors. Nat. Commun. **6**, 6828 (2015).

[11] M. Kunii, H. Iino, and J. Hanna, Solution-Processed, Low-Voltage Polycrystalline Organic Field-Effect Transistor Fabricated Using Highly Ordered Liquid Crystal With Low- k Gate Dielectric. IEEE Electron Device Lett. **37**, 486 (2016).

[12] T. Uemura, K. Nakayama, Y. Hirose, J. Soeda, M. Uno, W. Li, M. Yamagishi, Y. Okada, and J. Takeya, Band-like transport in solution-crystallized organic transistors. Curr. Appl. Phys. **12**, 87 (2012).

[13] H. Ebata, T. Izawa, E. Miyazaki, K. Takimiya, M. Ikeda, H. Kuwabara, and T. Yui, Highly Soluble [1] Benzothieno [3,2-b] benzothiophene (BTBT) Derivatives for High-Performance, Solution-Processed Organic Field-Effect Transistors. J. Am. Chem. Soc. **129**, 15732 (2007).

[14] T. Lei, J.Y. Wang, and J. Pei, Roles of flexible chains in organic semiconducting materials. Chem. Mater. **26**, 594 (2014).

[15] Y. Yamagishi, K. Noda, K. Kobayashi, and H. Yamada, Interlayer resistance and edge-specific charging in layered molecular crystals revealed by Kelvin-probe force microscopy. J. Phys. Chem. C **119**, 3006 (2015).

[16] P. V. Pesavento, R.J. Chesterfield, C.R. Newman, and C.D. Frisble, Gated four-probe measurements on pentacene thin-film transistors: Contact resistance as a function of gate voltage and temperature. J. Appl. Phys. **96**, 7312 (2004).

[17] P. V. Pesavento, K.P. Puntambekar, C.D. Frisbie, J.C. McKeen, and P.P. Ruden, Film and contact resistance in pentacene thin-film transistors: Dependence on film thickness, electrode geometry, and correlation with hole mobility. J. Appl. Phys. **99**, (2006).

[18] J. Takeya, M. Yamagishi, Y. Tominari, R. Hirahara, Y. Nakazawa, T. Nishikawa, T. Kawase, T. Shimoda, and S. Ogawa, Very high-mobility organic single-crystal transistors with in-crystal conduction channels. Appl. Phys. Lett. **90**, 2005 (2007).

[19] T. Uemura, C. Rolin, T.-H. Ke, P. Fesenko, J. Genoe, P. Heremans, and J. Takeya, On the Extraction of Charge Carrier Mobility in High-Mobility Organic Transistors. Adv. Mater. **28**, 151 (2015).

[20] A.C. Dürr, F. Schreiber, M. Münch, N. Karl, B. Krause, V. Kruppa, and H. Dosch, High structural order in thin films of the organic semiconductor diindenoperylene. Appl. Phys. Lett. **81**, 2276 (2002).

[21] R. Hayakawa, M. Petit, Y. Wakayama, and T. Chikyow, Evolution of quaterrylene thin films on a silicon dioxide surface using an ultraslow deposition technique. J. Phys. Chem. C **111**, 18703 (2007).

[22] D.G. de Oteyza, E. Barrena, S. Sellner, J.O. Osso, and H. Dosch, Molecular structure and growth morphologies of pentacene/fluorinated copper-phthalocyanine heterostructures. Thin Solid Films **516**, 7525 (2008).

[23] T.N. Krauss, E. Barrena, X.N. Zhang, D.G. de Oteyza, J. Major, V. Dehm, F. Würthner, L.P. Cavalcanti, and H. Dosch, Three-dimensional molecular packing of thin organic films of PTCDI-C8 determined by surface X-ray diffraction. Langmuir **24**, 12742 (2008).

[24] R. Rahimi, V. Narang, and D. Korakakis, Optical and morphological studies of thermally evaporated PTCDI-C8 thin films for organic solar cell applications. Int. J. Photoenergy **2013**, (2013).

[25] C. Ranacher, R. Resel, P. Moni, B. Cermenek, V. Hacker,

and A.M. Coclite, Layered Nanostructures in Proton Conductive Polymers Obtained by Initiated Chemical Vapor Deposition. Macromolecules **48**, 6177 (2015).

[26] D. Chandler-Horowitz and P.M. Amirtharaj, High-accuracy, midinfrared (450 cm^{−1} leq ω leq4000 cm^{-1}) refractive index values of silicon. J. Appl. Phys. **97**, 123526 (2005).

[27] I.H.Malitson, Imterspecimen Comparison of the Refractive Index of Fused Silica. J. Opt. Soc. Am. **55**, 1205 (1965).

[28] D.J. Gundlach, L. Zhou, J. a. Nichols, T.N. Jackson, P. V. Necliudov, and M.S. Shur, An experimental study of contact effects in organic thin film transistors. J. Appl. Phys. **100**, 24509 (2006).

[29] D. Kumaki, Y. Fujisaki, and S. Tokito, Reduced contact resistance and highly stable operation in polymer thin-film transistor with aqueous MoOx solution contact treatment. Org. Electron. Physics, Mater. Appl. **14**, 475 (2013).

[30] M. Kitamura, Y. Kuzumoto, S. Aomori, M. Kamura, J.H. Na, and Y. Arakawa, Threshold voltage control of bottom-contact n-channel organic thin-film transistors using modified drain/source electrodes. Appl. Phys. Lett. **94**, 83310 (2009).

[31] K. Aoshima, S. Arai, K. Fukuhara, T. Yamada, and T. Hasegawa, Surface modification of printed silver electrodes for efficient carrier injection in organic thin-film transistors. Org. Electron. **41**, 137 (2016).

[32] Y. Xu, T. Minari, K. Tsukagoshi, J.A. Chroboczek, and G. Ghibaudo, Direct evaluation of low-field mobility and access resistance in pentacene field-effect transistors. J. Appl. Phys. **107**, 114507 (2010).

[33] S. Fabiano, C. Musumeci, Z. Chen, A. Scandurra, H. Wang, Y.L. Loo, A. Facchetti, and B. Pignataro, From monolayer to multilayer n-channel polymeric field-effect transistors with precise conformational order. Adv. Mater. **24**, 951 (2012).

[34] A. Sharma, F.W.A. van Oost, M. Kemerink, and P.A. Bobbert, Dimensionality of charge transport in organic field-effect transistors. Phys. Rev. B **85**, 235302 (2012).

[35] K.P. Puntambekar, P. V. Pesavento, and C.D. Frisbie, Surface potential profiling and contact resistance measurements on operating pentacene thin-film transistors by Kelvin probe force microscopy. Appl. Phys. Lett. **83**, 5539 (2003).

[36] S.G.J. Mathijssen, E.C.P. Smits, P. a van Hal, H.J. Wondergem, S. a Ponomarenko, A. Moser, R. Resel, P. a Bobbert, M. Kemerink, R. a J. Janssen, and D.M. de Leeuw, Monolayer coverage and channel length set the mobility in self-assembled monolayer field-effect transistors. Nat. Nanotechnol. **4**, 674 (2009).

[37] J.G. Simmons, Generalized Formula for the Electric Tunnel Effect between Similar Electrodes Separated by a Thin Insulating Film. J. Appl. Phys. **34**, 1793 (1963).

[38] W. Wang, T. Lee, and M.A. Reed, Mechanism of electron conduction in self-assembled alkanethiol monolayer devices. Phys. Rev. B **68**, 35416 (2003).

[39] T. Lee, W. Wang, J.F. Klemic, J.J. Zhang, J. Su, and M.A. Reed, Comparison of Electronic Transport Characterization Methods for Alkanethiol Self-Assembled Monolayers. J. Phys. Chem. B **108**, 8742 (2004).

[40] A. Salomon, T. Boecking, C.K. Chan, F. Amy, O. Girshevitz, D. Cahen, and A. Kahn, How do electronic carriers cross Si-bound alkyl monolayers? Phys. Rev. Lett. **95**, 266807 (2005).

[41] A. Salomon, H. Shpaisman, O. Seitz, T. Boecking, and D. Cahen, Temperature-Dependent Electronic Transport through Alkyl Chain Monolayers : Evidence for a Molecular Signature Temperature-Dependent Electronic Transport through Alkyl Chain Monolayers : Evidence for a Molecular Signature. J. Phys. Chem. C **112**, 3969 (2008).

[42] E.A. Weiss, R.C. Chiechi, G.K. Kaufman, J.K. Kriebel, Z. Li, M. Duati, M.A. Rampi, and G.M. Whitesides, Influence of defects on the electrical characteristics of mercury-drop junctions: Self-assembled monolayers of n-alkanethiolates on rough and smooth silver. J. Am. Chem. Soc. **129**, 4336 (2007).

[43] M.M. Thuo, W.F. Reus, C.A. Nijhuis, J.R. Barber, C. Kim, M.D. Schulz, and G.M. Whitesides, Odd-even effects in charge transport across self-assembled monolayers J. Am. Chem. Soc. **133**, 2962 (2011).

[44] J.G. Simmons, Low-voltage current-voltage relationship of tunnel junctions. J. Appl. Phys. **34**, 238 (1963).

[45] T.J. Richards and H. Sirringhaus, Analysis of the contact resistance in staggered, top-gate organic field-effect transistors.

J. Appl. Phys. **102**, 1 (2007).

[46] Y. Diao, B.C.-K. Tee, G. Giri, J. Xu, D.H. Kim, H. a Becerril, R.M. Stoltenberg, T.H. Lee, G. Xue, S.C.B. Mannsfeld, and Z. Bao, Solution coating of large-area organic semiconductor thin films with aligned single-crystalline domains. Nat. Mater. **12**, 665 (2013).

FIG. 1. (a) Schematic for blade-coating process. (b) Optical microscopy image of single-crystalline thin film. (c,d) Crossed-Nicol polarized micrographs of (b). Scale bar is 1 mm.

FIG. 2. (a) A micrograph of a single-crystal film with thickness variation. The observed color variation is due to the molecular-level thickness variation. (b) A cross-sectional height profile observed by AFM. No step was observed in the mono-colored area of the film, but multiple bilayer steps was found where the color change at the border between ocher-colored and light-blue-colored area. The inset is an expanded micrograph of (a) around the border. Scale bar: (a) 200 μm, (b) 50 μm.

FIG. 3. (a) Schematic for the diffraction experiment. (b) Cross-sectional height profile of a single-crystalline film with thickness of n = 8 bilayer-thickness, and the micrograph (inset). (c) Diffractograms of the films with thickness of n = 6, 7, 8 on SiO2/Si substrates, and the diffraction intensity profile for the film of n = 8. (d) Diffraction intensity profile of the film of n = 5 on Si substrate without silica layer. The observed Laue fringes are clearer due to the absence of x-ray scattering of silica layer. Scale bar in (c) is 1 mm.

FIG. 4. Optical image of single-crystalline thin film with (a) 1 bilayer, (b) 5 bilayers, (c) 10 bilayers, and (d) 14bilayers. Scale bars are 1 mm.

FIG. 5. (a) Model of multiple reflection. (b) Calculated reflectivity of Ph-BTBT-C10 single-crystalline thin film on Si/SiO2 substrate for R (700 nm), G (550 nm), and B (440 nm). The inset shows the corresponding colors.

FIG. 6. Device characteristics of Ph-BTBT-C_{10} single-crystalline OTFTs with different layer-number thickness. Output characteristics (a-c) and transfer characteristics (d-f) for the OTFTs with thickness of (a, d) n = 2, (b, e) n = 6, and (c, f) n = 15. Drain voltage applied in the transfer characteristics measurements are −10 V, −15 V, and −15 V, respectively.

FIG. 7. Tunneling transport and layer-number dependence of injection voltage and device mobility. (a) Measured (solid curves) and simulated (broken curves) normalized output characteristics (solid curve) for Ph-BTBT-C10 single-crystalline OTFTs with a variety of layer-number thickness. (b) Layer-number dependence of injection voltage (V_{inj}) and (c) device mobility in linear regime. (d) Schematic for interlayer access resistance caused by insulating alkyl chain layers.

FIG. 8. (a) Microscope image of a device for gated-four-probe measurement. Scale bar is 1 mm. (b) Transfer characteristics obtained by gated-four-probe measurement obtained with a OTFT with 3 bilayers film at V_d = −15 V. Inset shows gate voltage dependence of channel resistance (red broken line) and parasitic resistance on source (blue) and drain electrodes (green). (c) Device mobility (μ_{lin}, black curve) and gated-four-probe mobility (μ_{gFPP}, red curve), derived by the first derivatives of transfer curves, are plotted as a function of V_g. (d) Layer-number dependence of μ_{gFPP}. The broken line indicates the intrinsic mobility estimated by the layer-number dependence of μ_{lin}.

FIG. 9. (a) The shape of electrode. (b) Schematic cross-sectional view of carrier injection.

Tab. 1 Parameters of layer number dependence

Tab. 2 Channel resistance (R_{ch}) and access resistance obtained from layer number dependence of device mobility (μ-n), gated-four-probe measurement (gFPP), and numerical simulation. [a]: at V_g=40 V in Fig. 8(b). [b]: at 0.7 V.

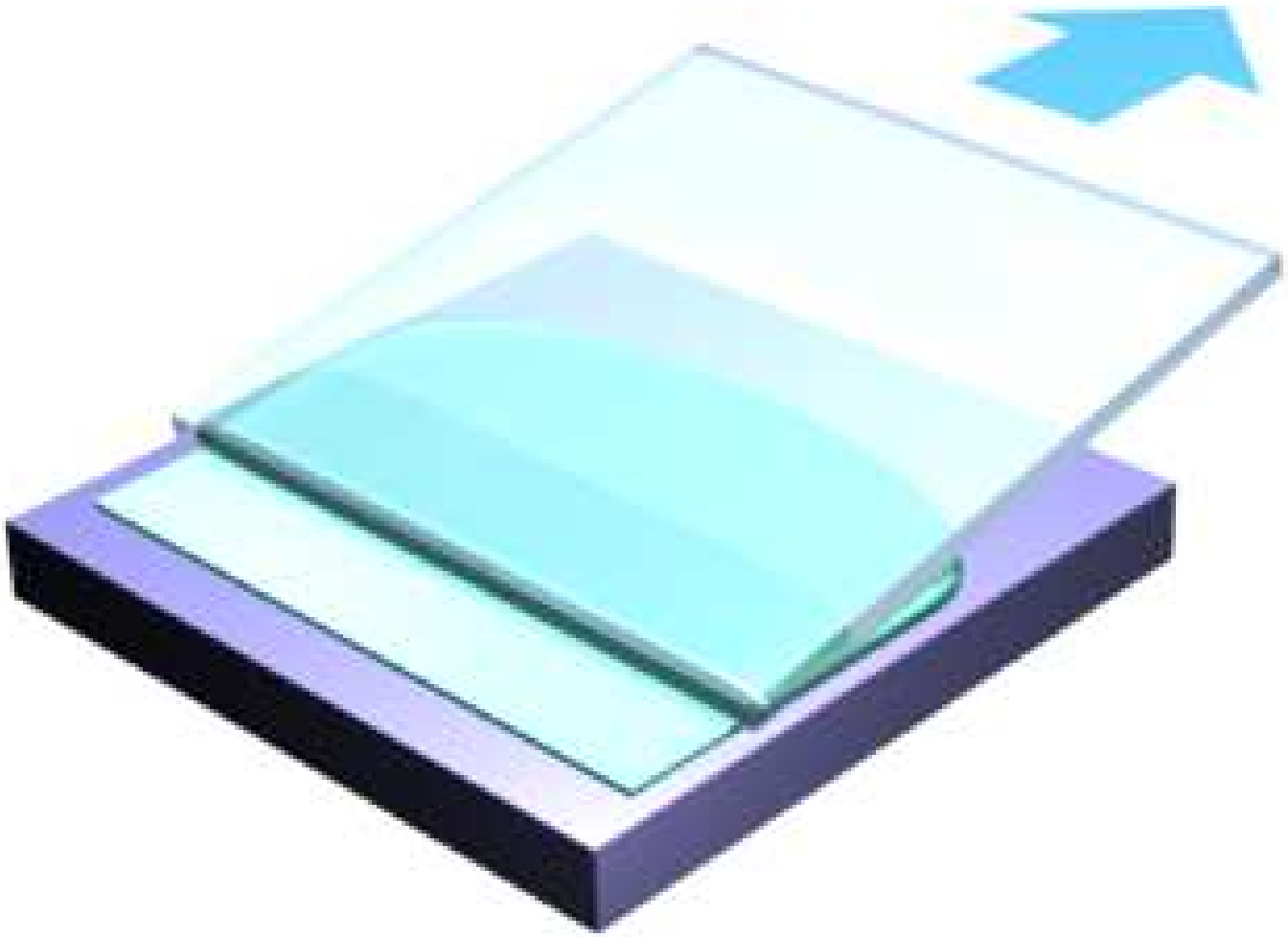

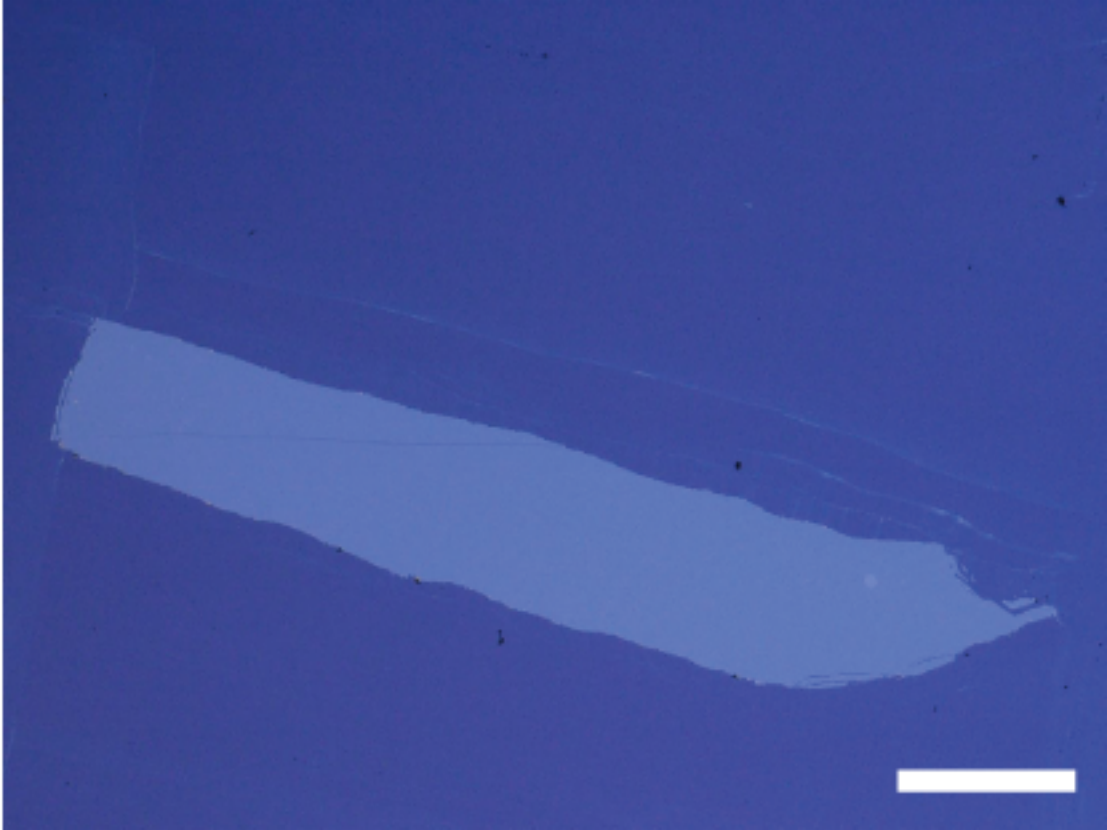

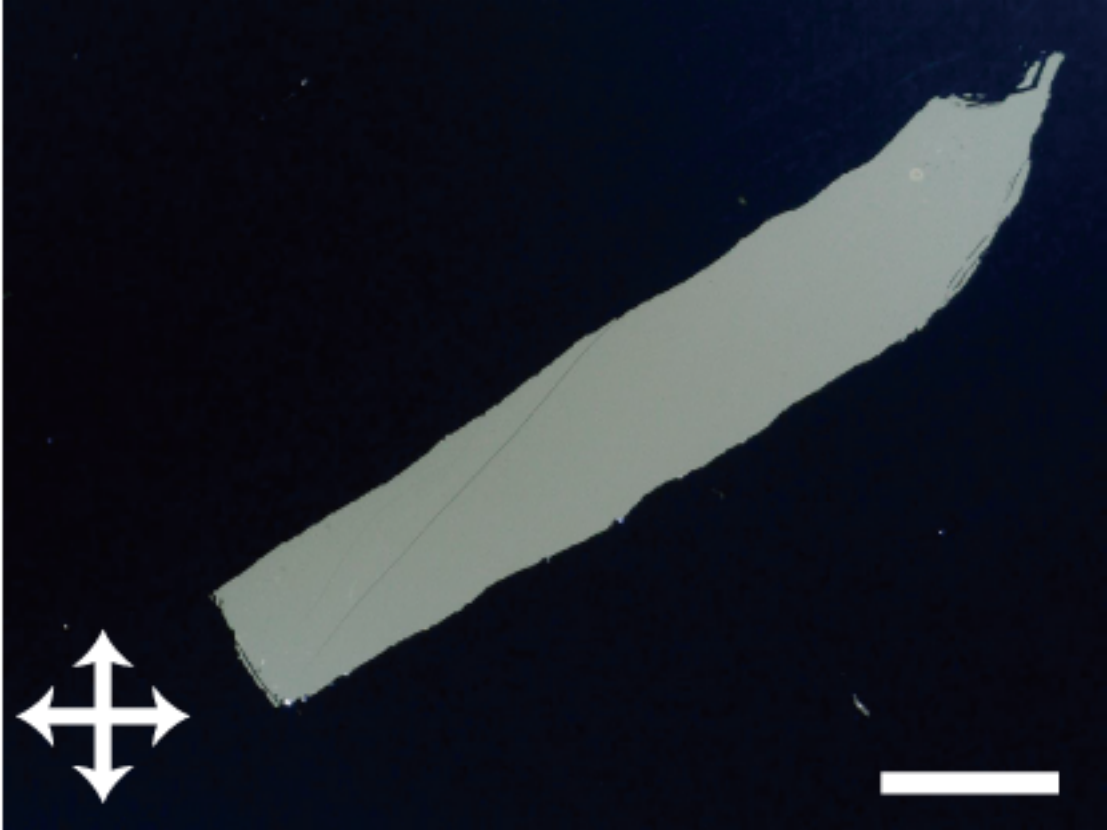

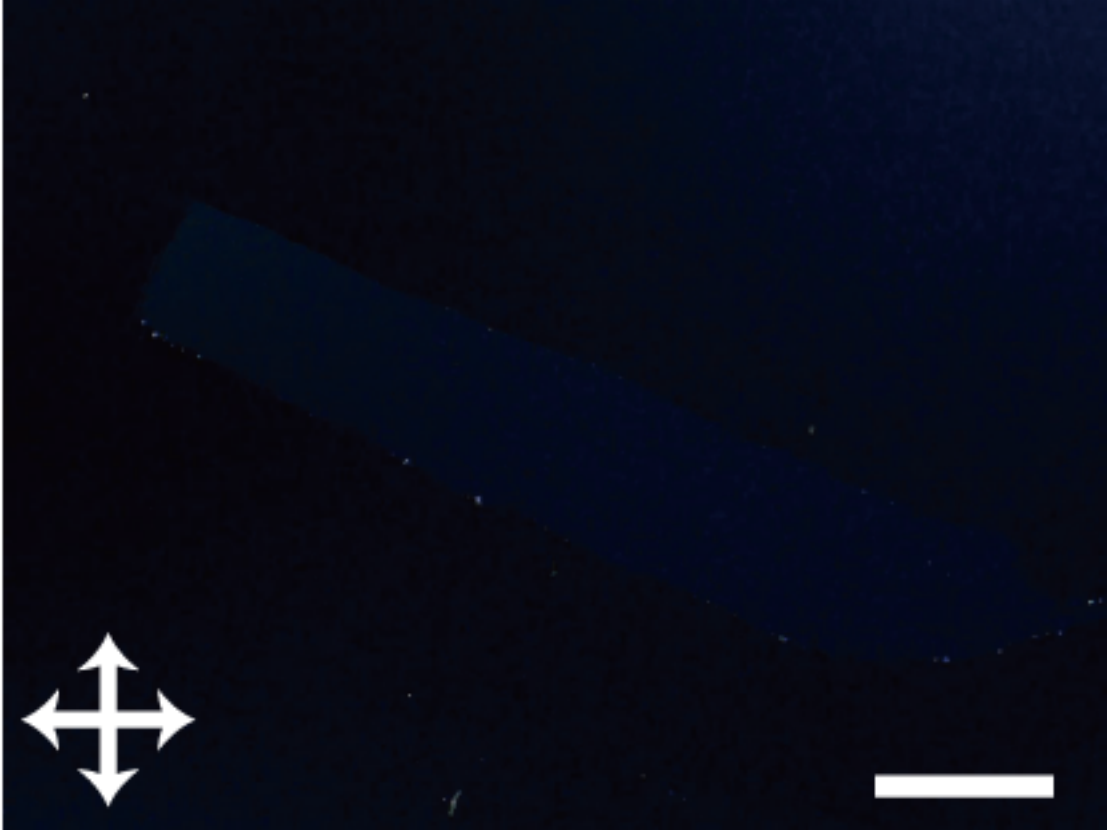

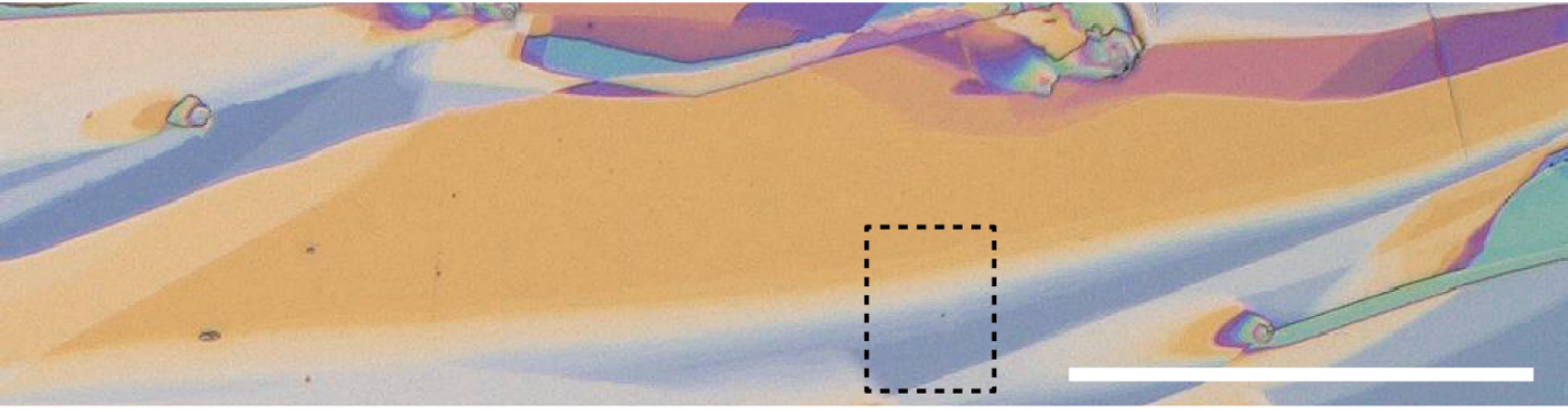

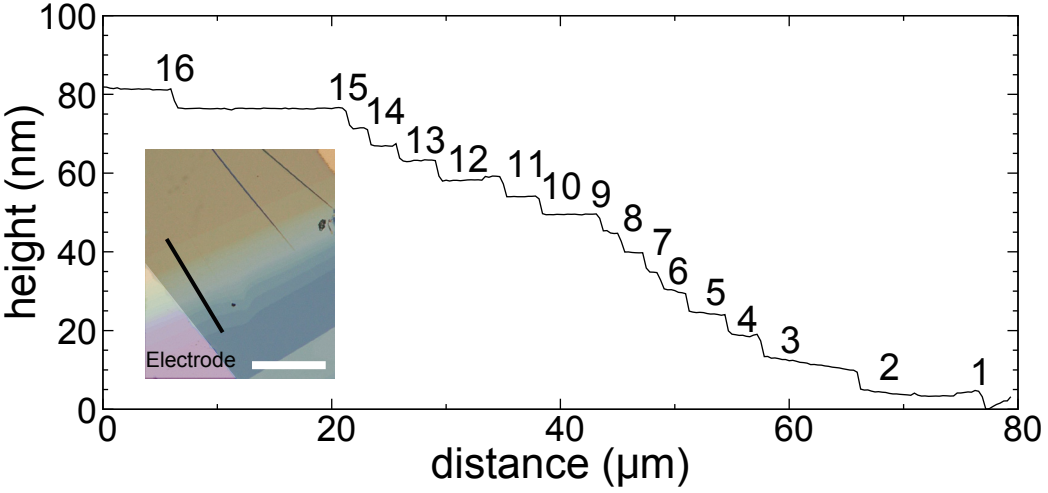
height (nm)
distance (μm)
0
20
40
60
80
100
16
15
14
13
12
11
10
9
8
7
6
5
4
3
2
1
Electrode

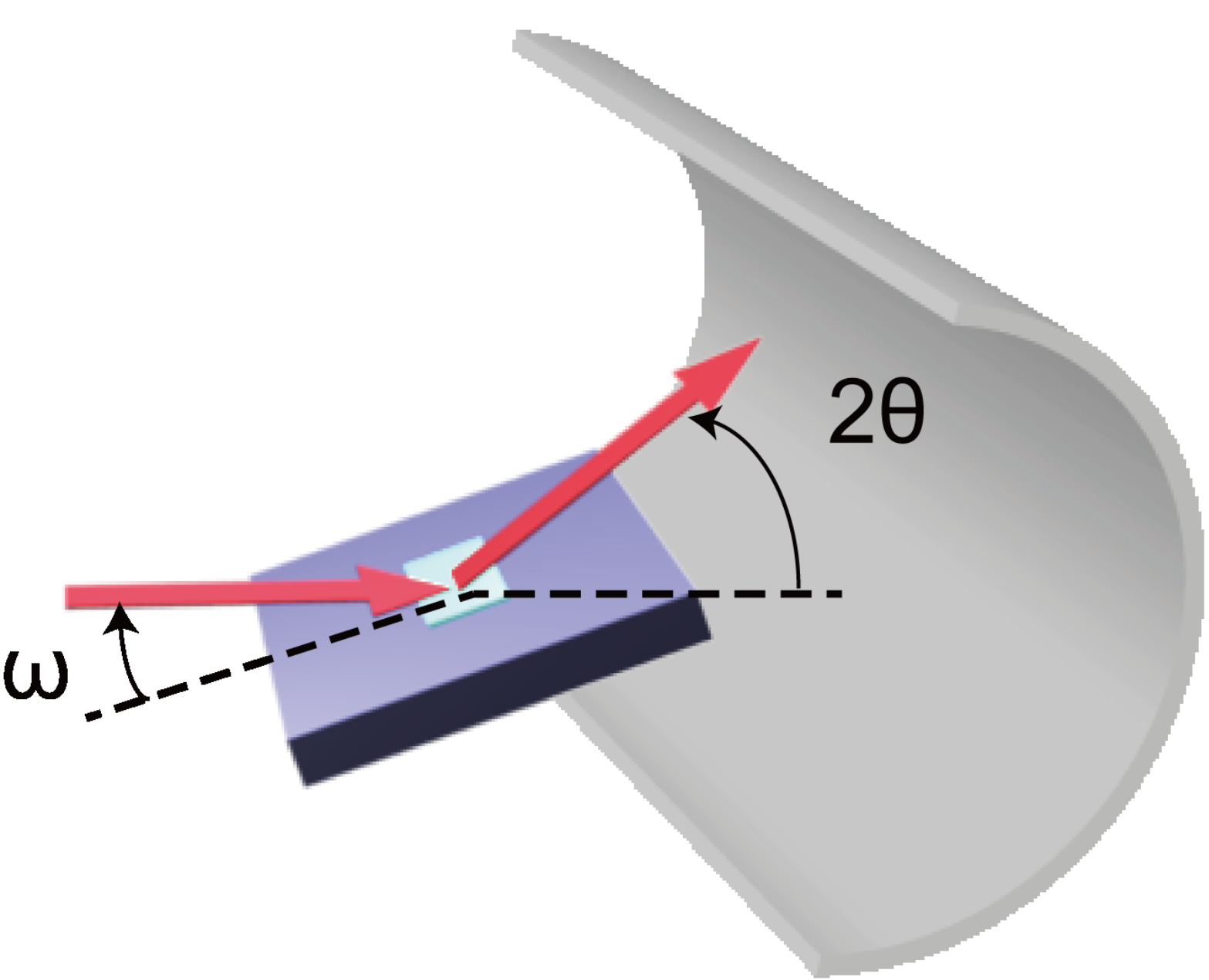
2θ
ω

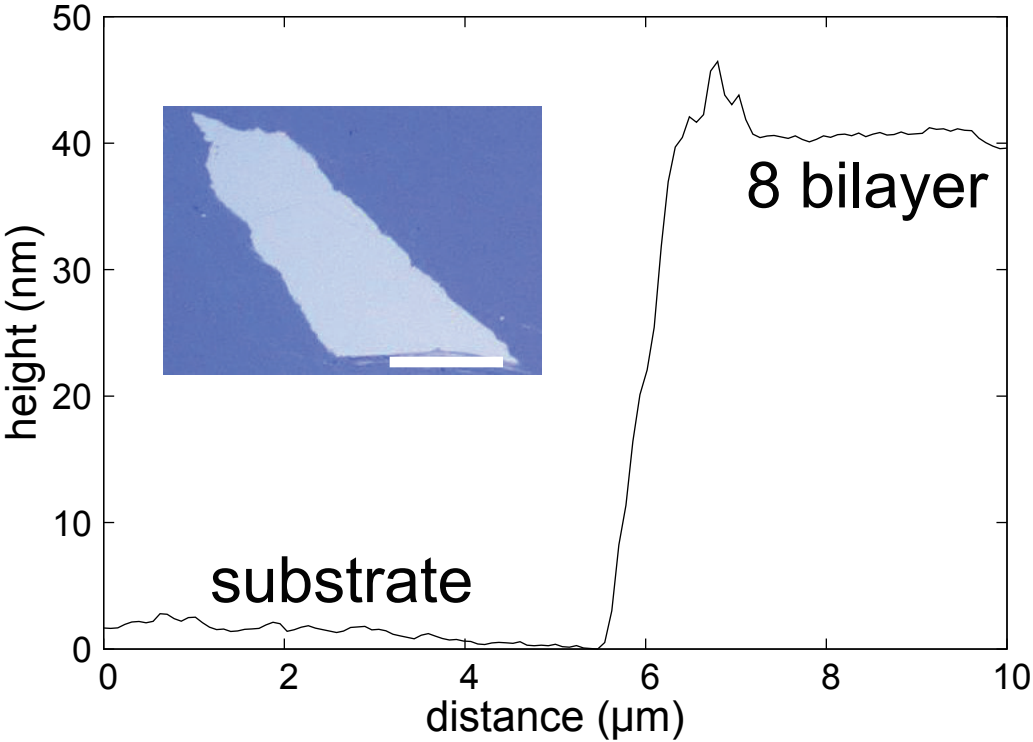
50
40
30
20
10
0
height (nm)
0
2
4
6
8
10
distance (μm)
8 bilayer
substrate

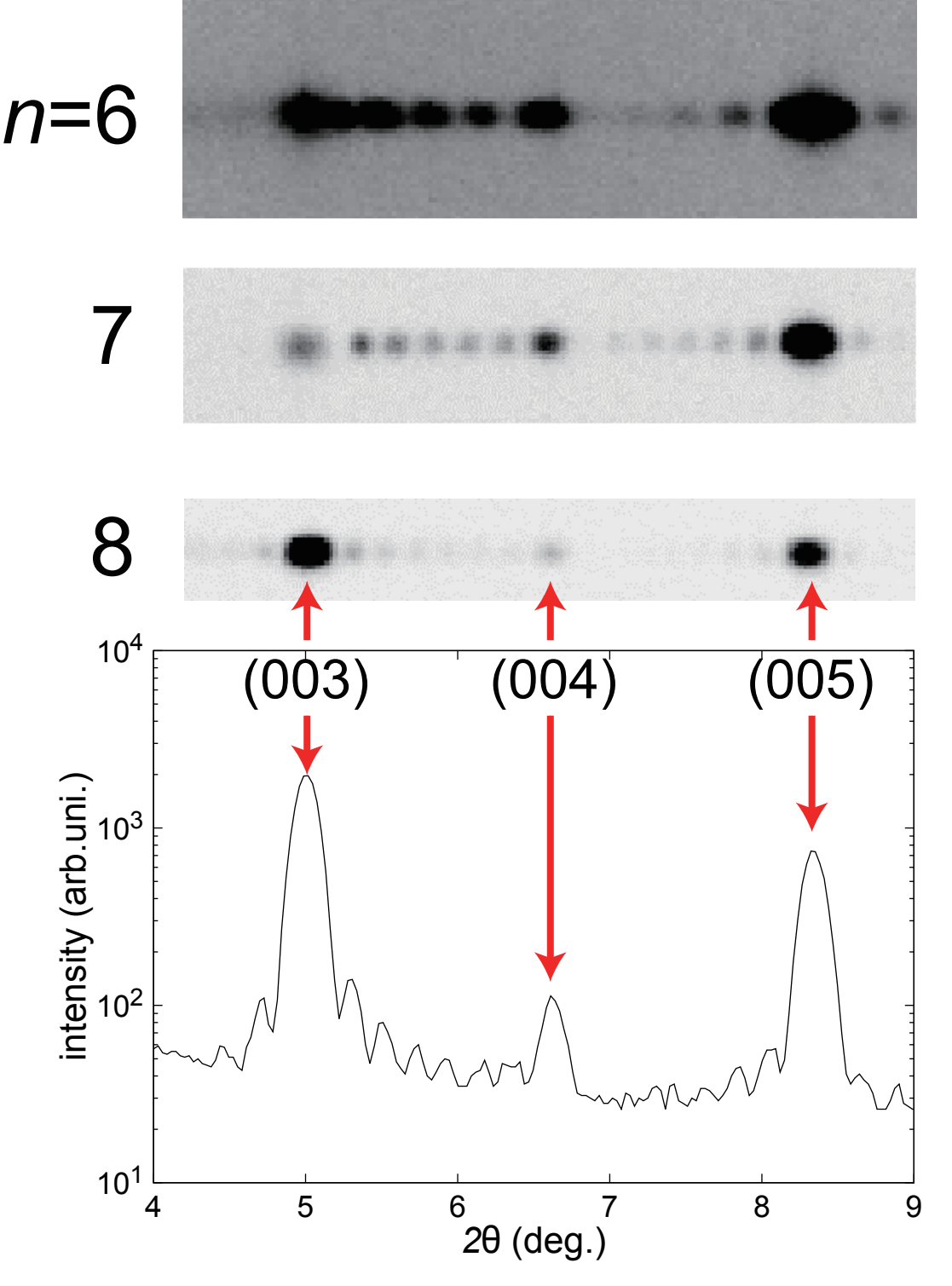
n=6
7
8
(003)
(004)
(005)
intensity (arb.uni.)
10^4
10^3
10^2
10^1
4
5
6
7
8
9
2θ (deg.)

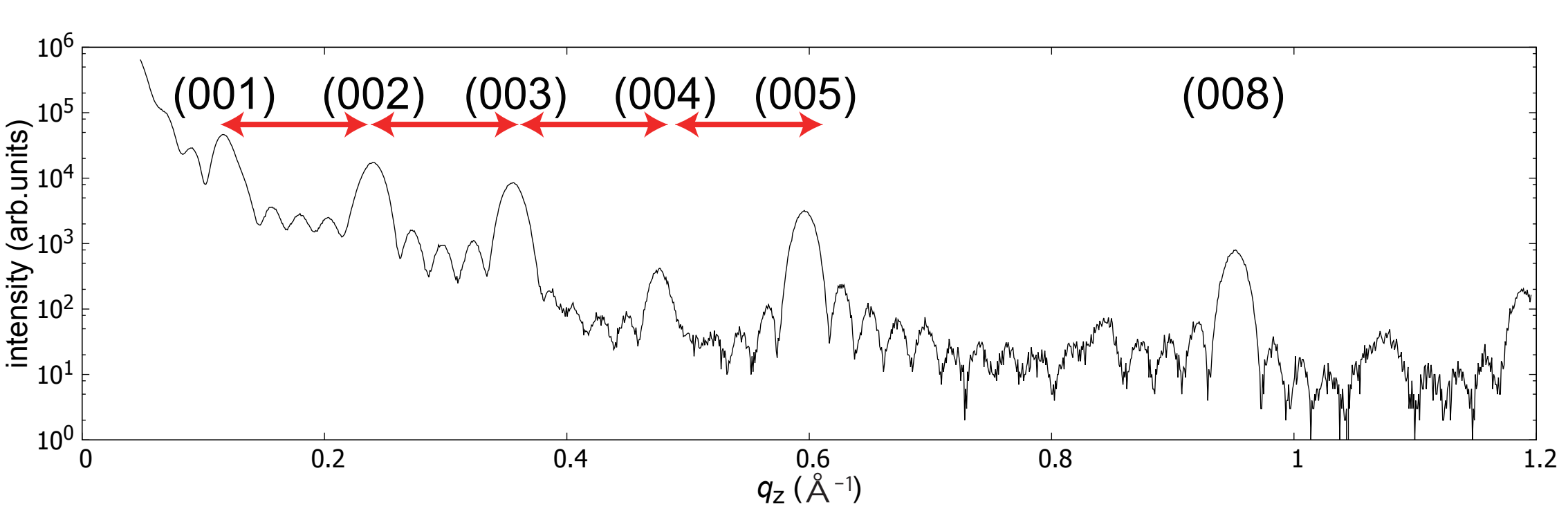
(001)
(002)
(003)
(004)
(005)
(008)
intensity (arb.units)
10^0
10^1
10^2
10^3
10^4
10^5
10^6
0
0.2
0.4
0.6
0.8
1
1.2
q_z (Å^{-1})


1 bilayer


5 bilayers

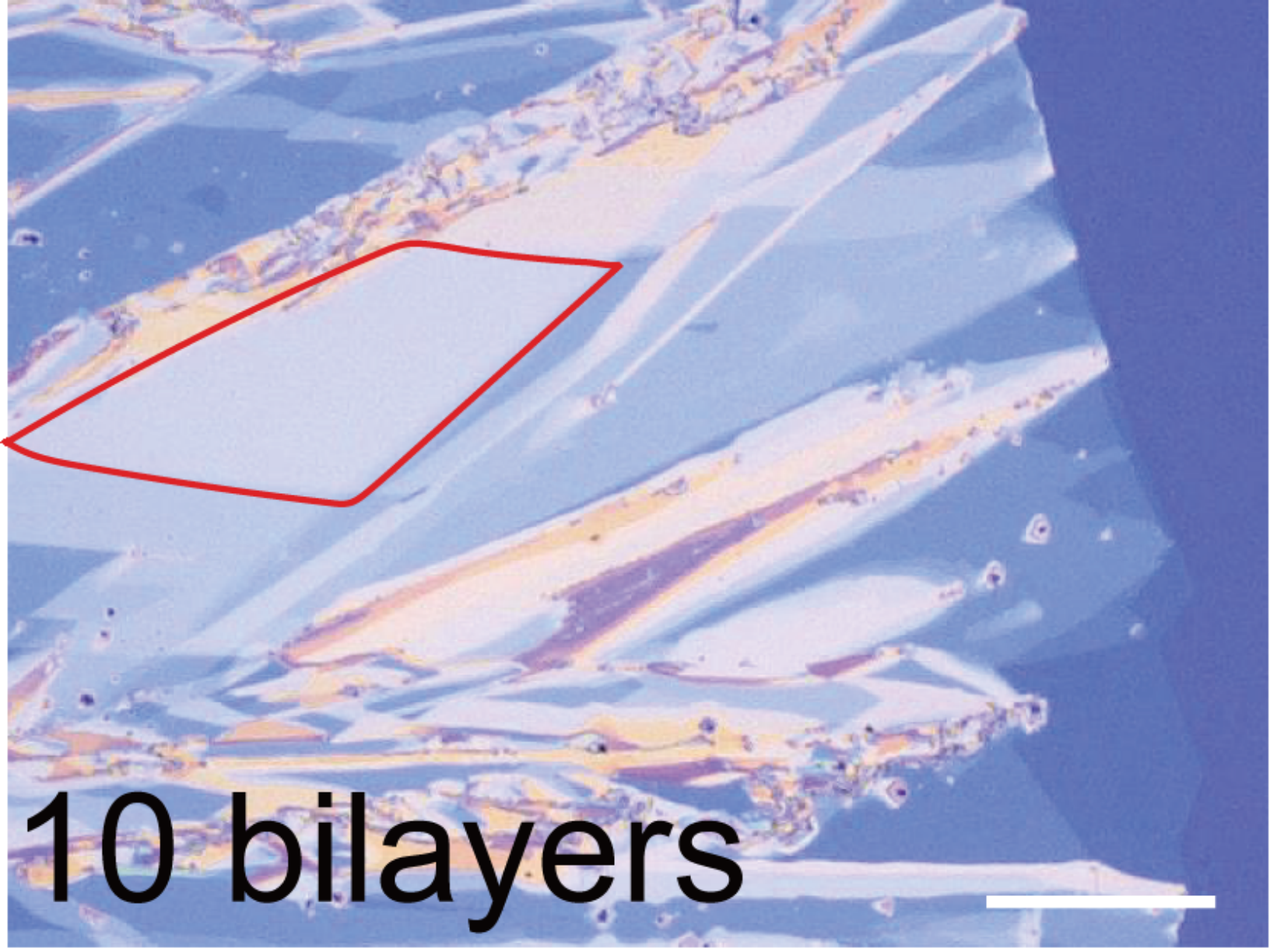
10 bilayers

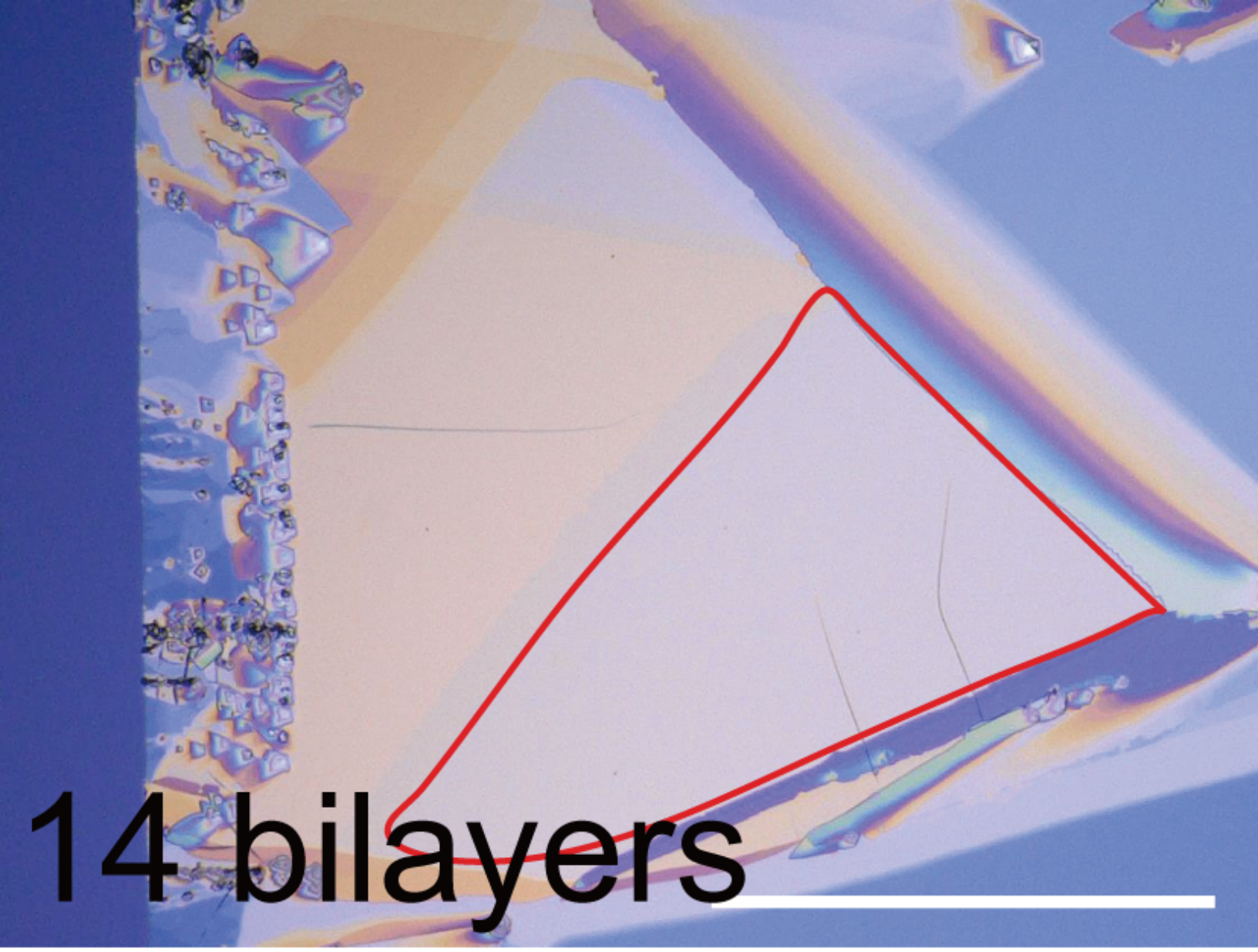
14 bilayers

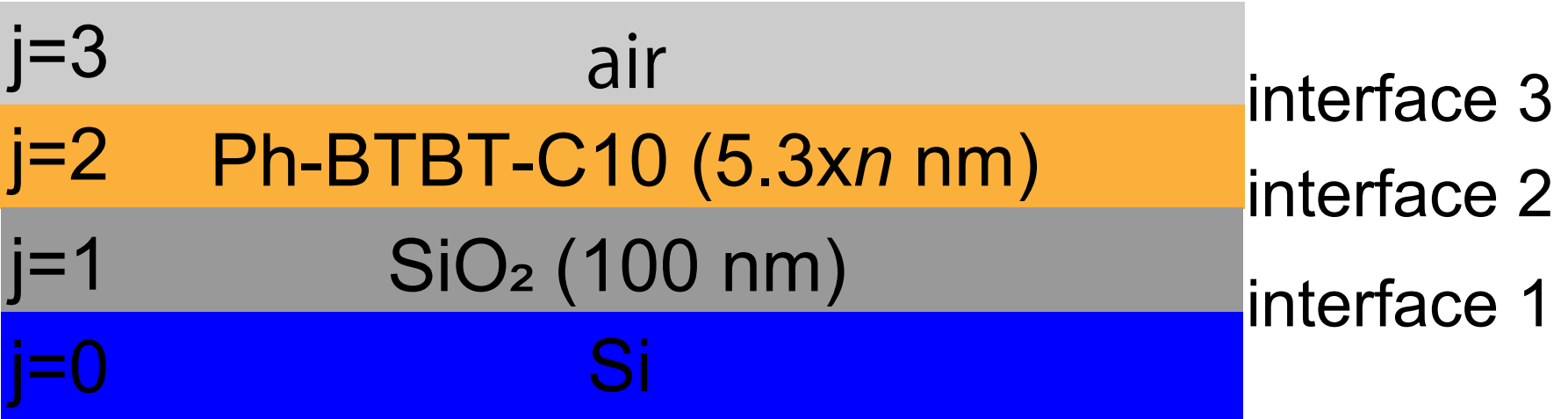
j=3
air
j=2
Ph-BTBT-C10 (5.3x*n* nm)
j=1
SiO₂ (100 nm)
j=0
Si
interface 3
interface 2
interface 1

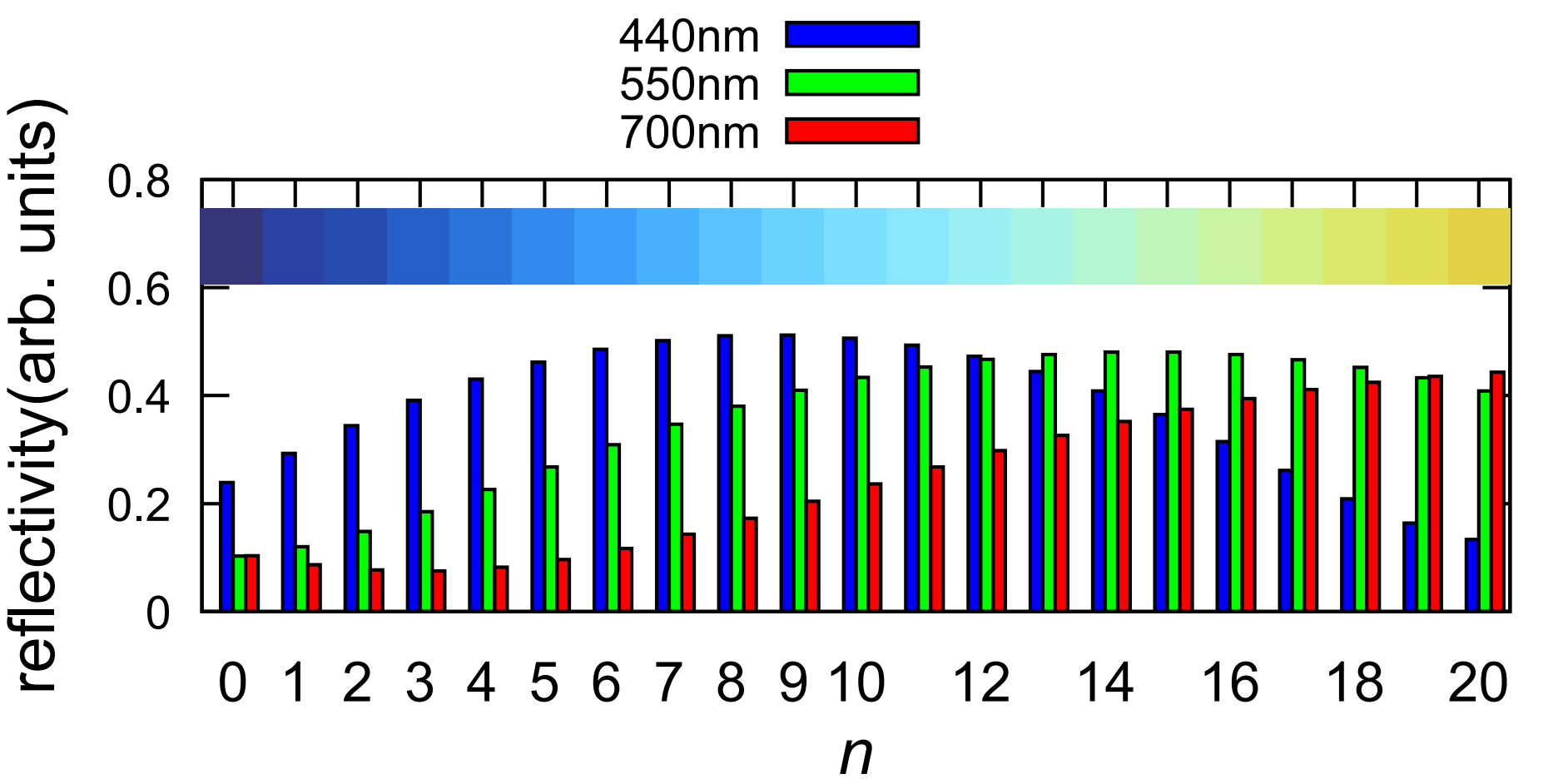
440nm
550nm
700nm
reflectivity(arb. units)
0.8
0.6
0.4
0.2
0
0 1 2 3 4 5 6 7 8 9 10 12 14 16 18 20
n

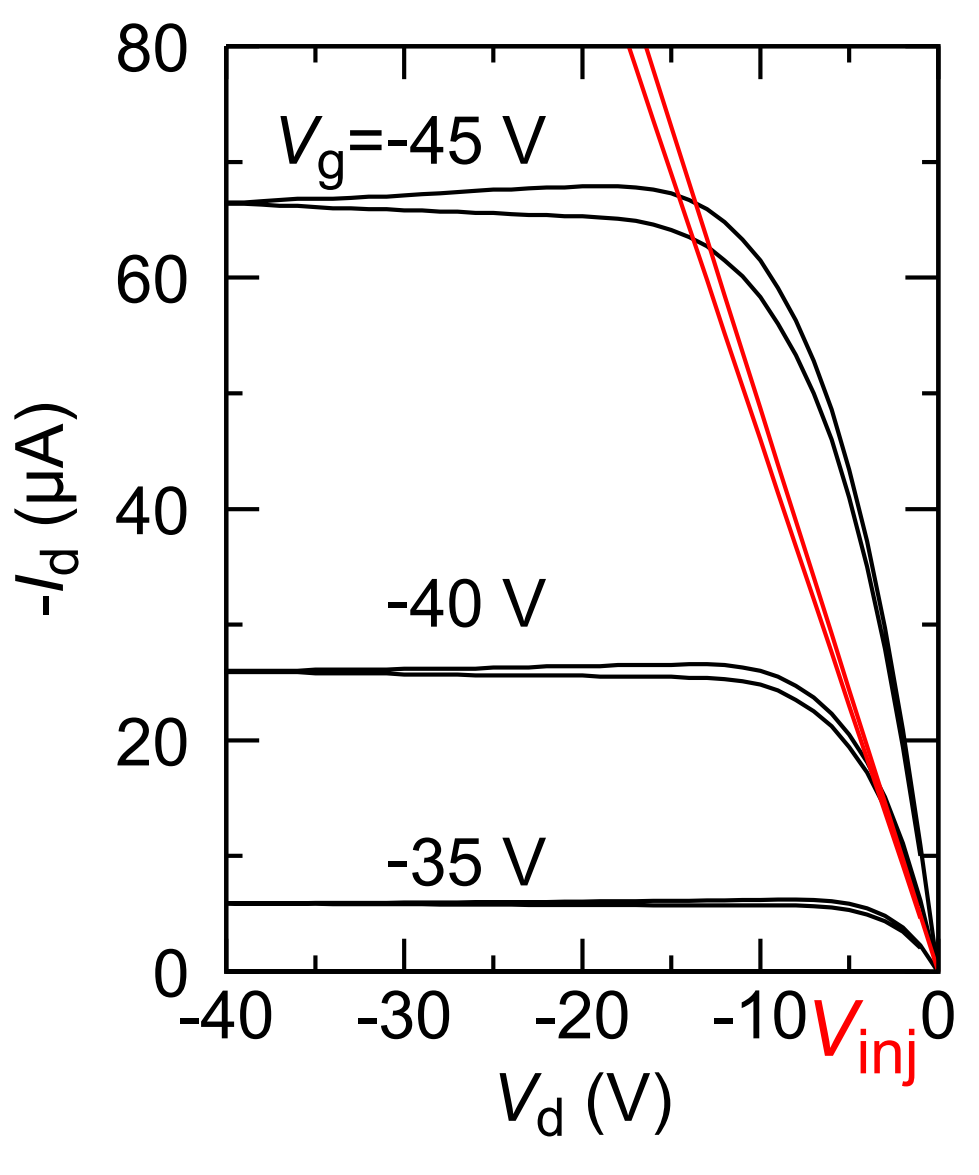
80
60
40
20
0
$-I_d$ (μA)
V_g=-45 V
-40 V
-35 V
-40
-30
-20
-10
0
V_{inj}
V_d (V)

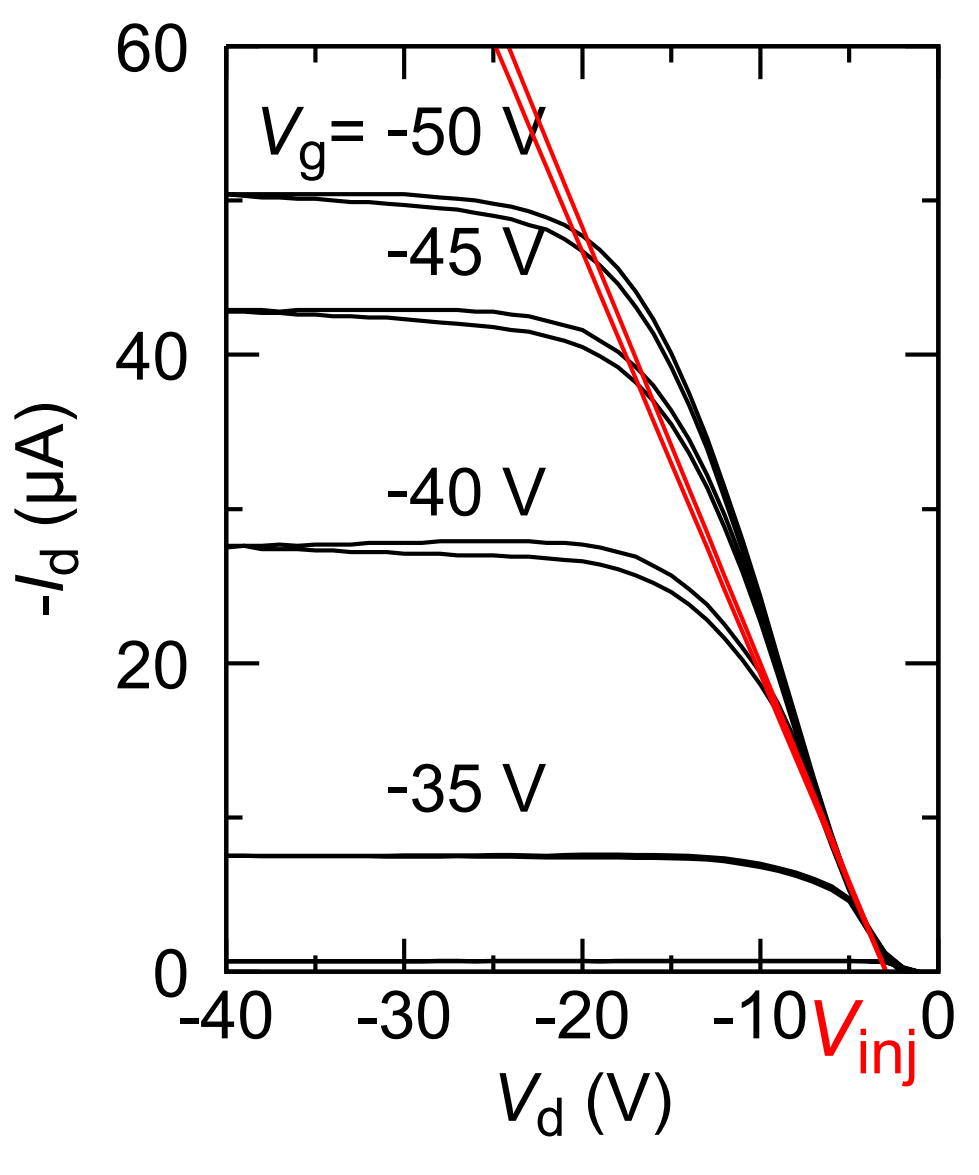
60
40
20
0
-40
-30
-20
-10
0
V_g= -50 V
-45 V
-40 V
-35 V
V_{inj}
$-I_d$ (μA)
V_d (V)

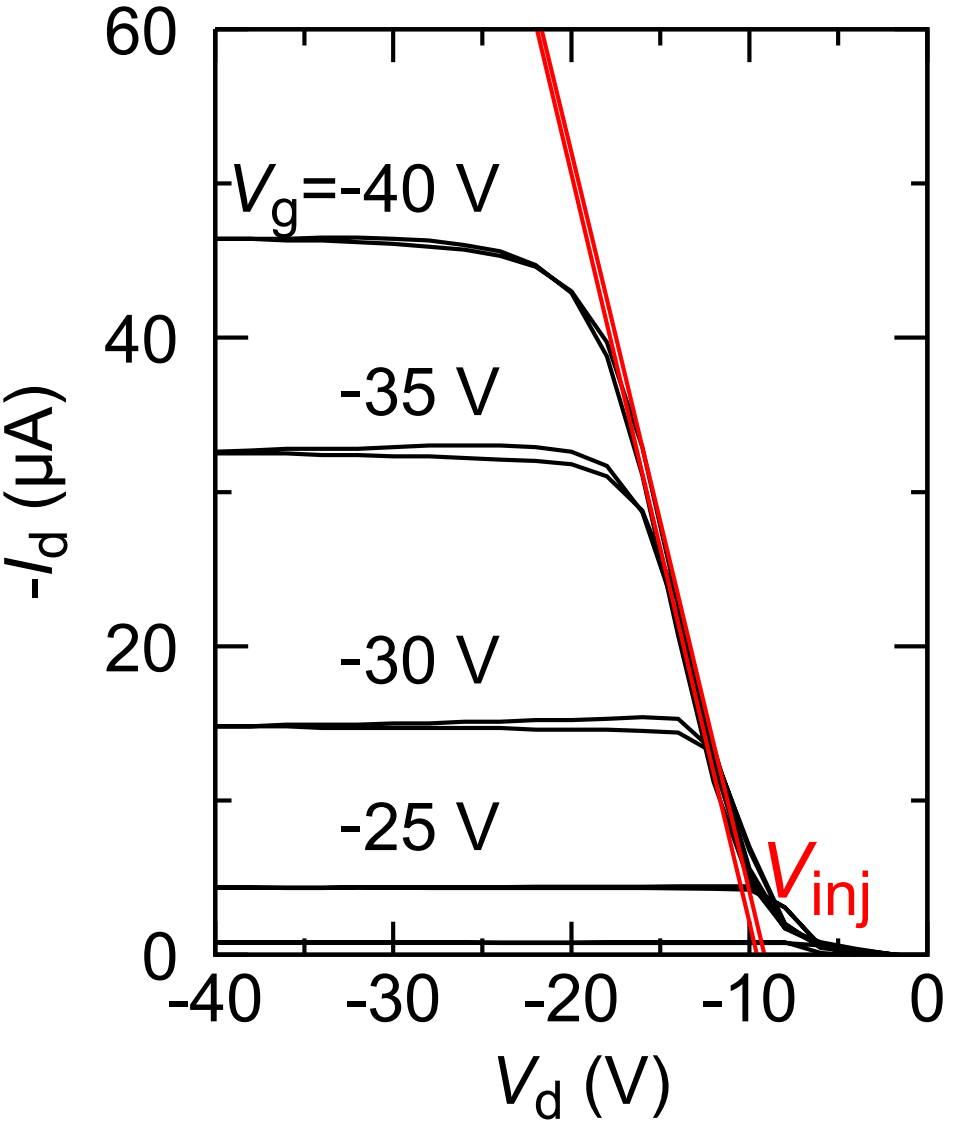
60
40
20
0
-40
-30
-20
-10
0
$-I_d$ (μA)
V_d (V)
V_g=-40 V
-35 V
-30 V
-25 V
V_{inj}

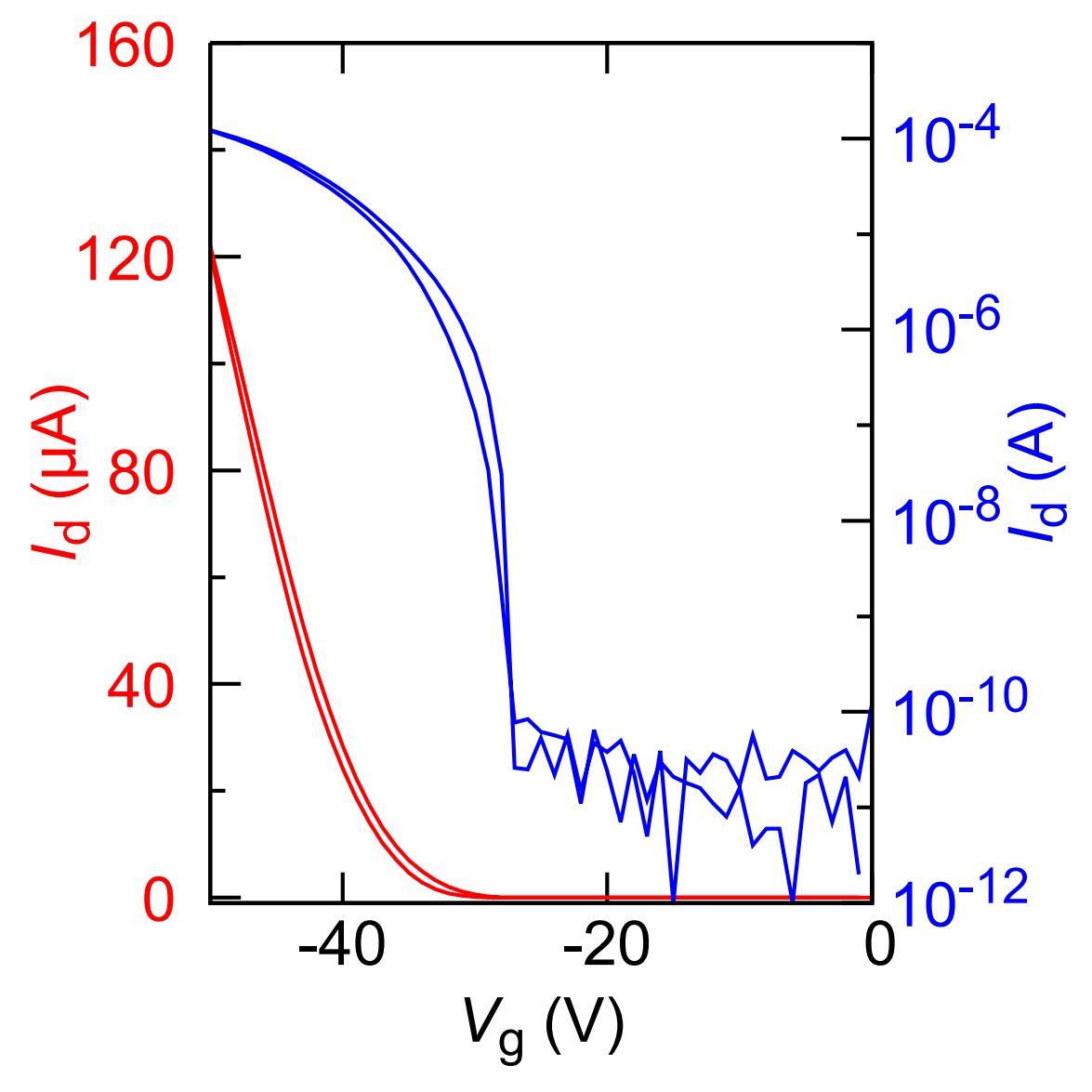
160
120
80
40
0
I_d (μA)
10^{-4}
10^{-6}
10^{-8}
10^{-10}
10^{-12}
I_d (A)
-40
-20
0
V_g (V)

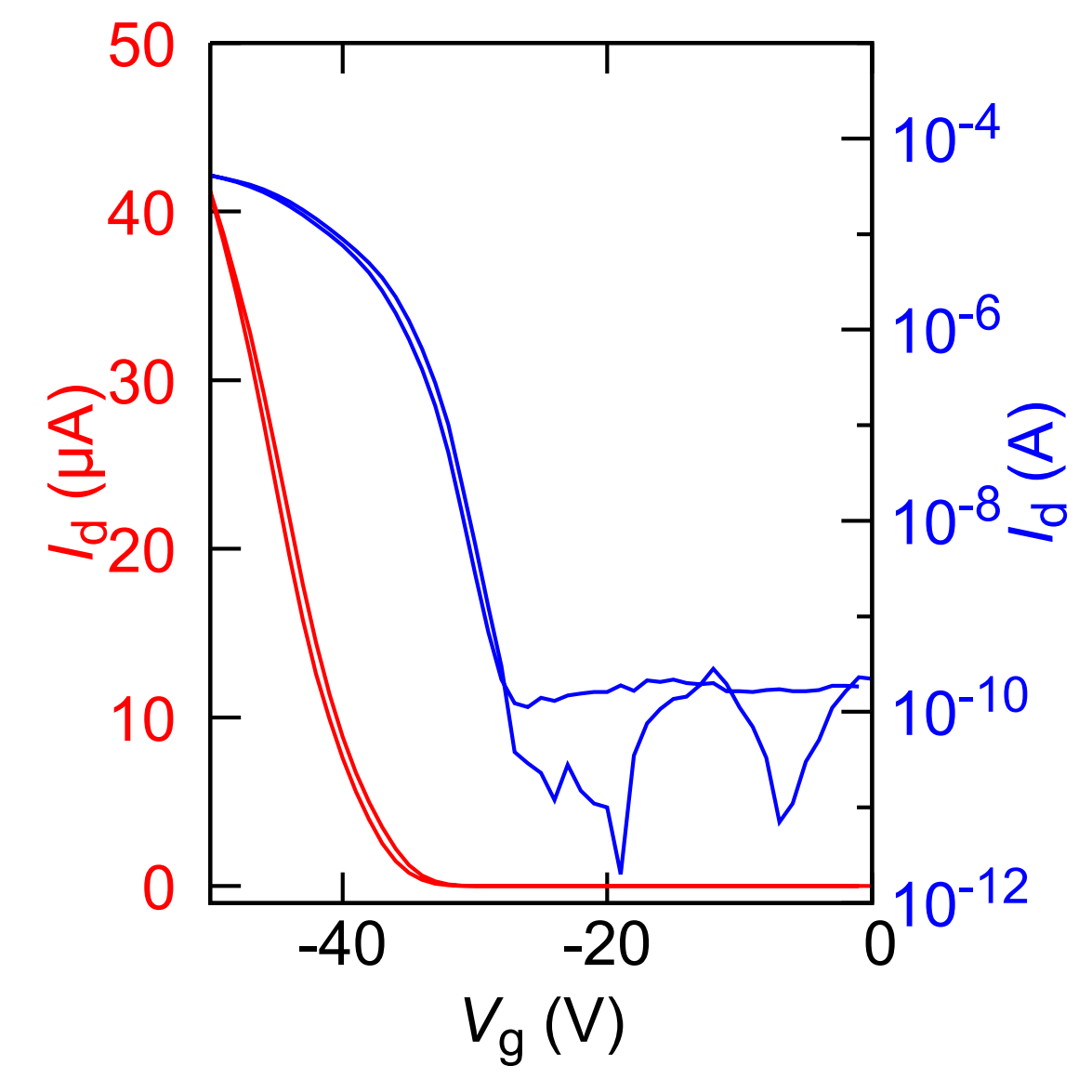
50
40
30
20
10
0
I_d (μA)
10^{-4}
10^{-6}
10^{-8}
10^{-10}
10^{-12}
I_d (A)
-40
-20
0
V_g (V)

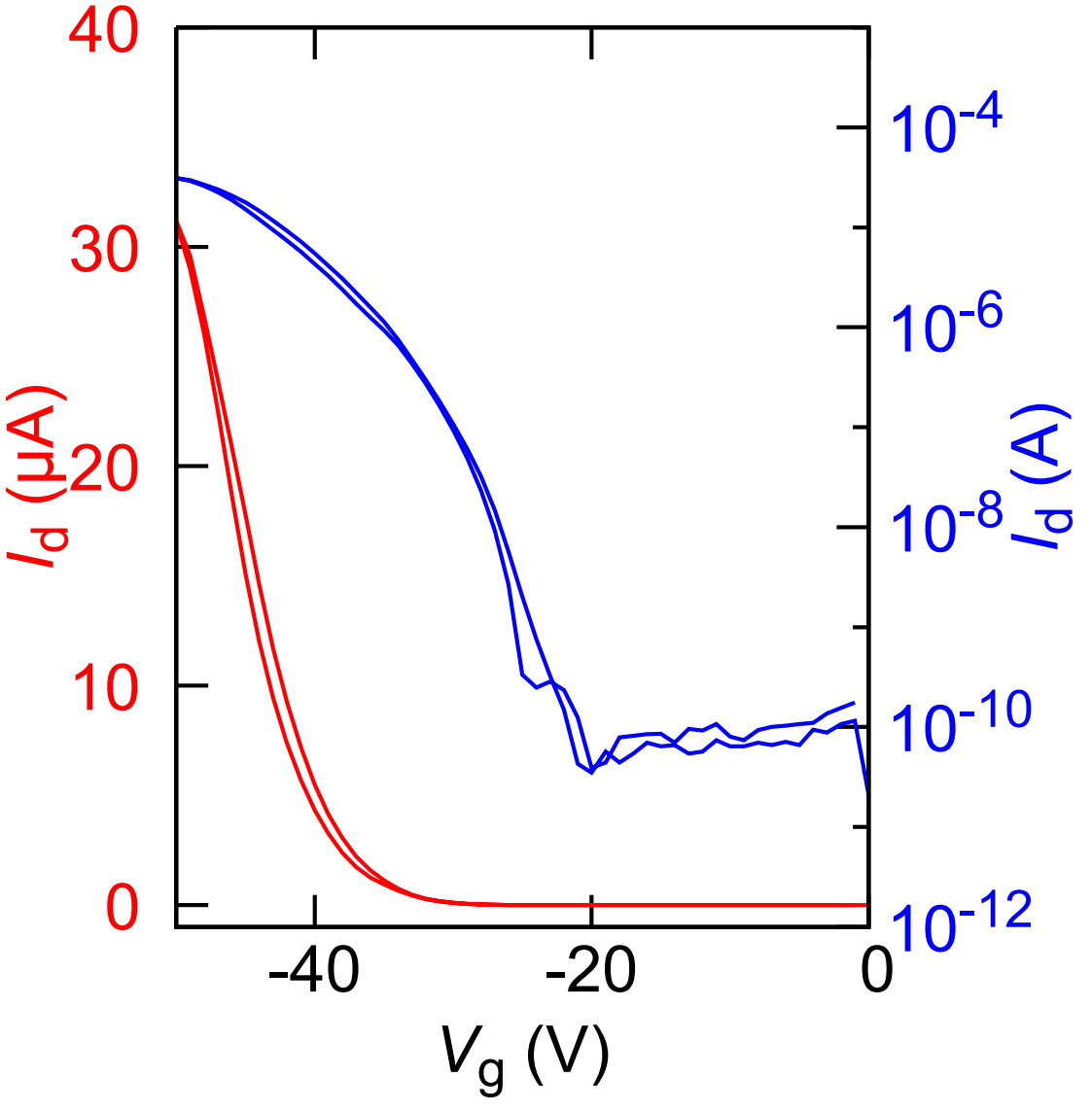
40
30
20
10
0
I_d (μA)
10^{-4}
10^{-6}
10^{-8}
10^{-10}
10^{-12}
I_d (A)
-40
-20
0
V_g (V)

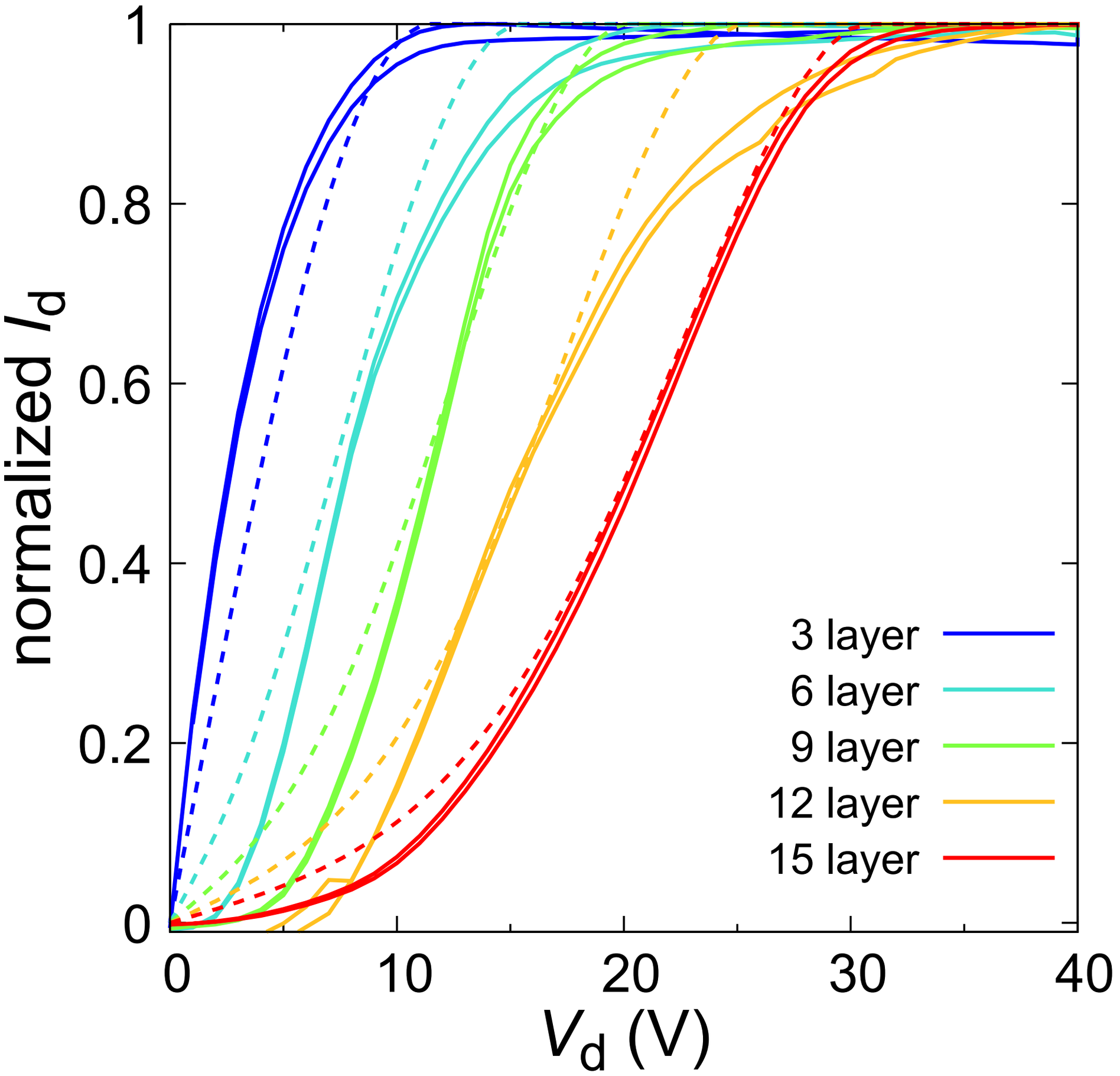
normalized I_d
1
0.8
0.6
0.4
0.2
0
0
10
20
30
40
V_d (V)
3 layer
6 layer
9 layer
12 layer
15 layer

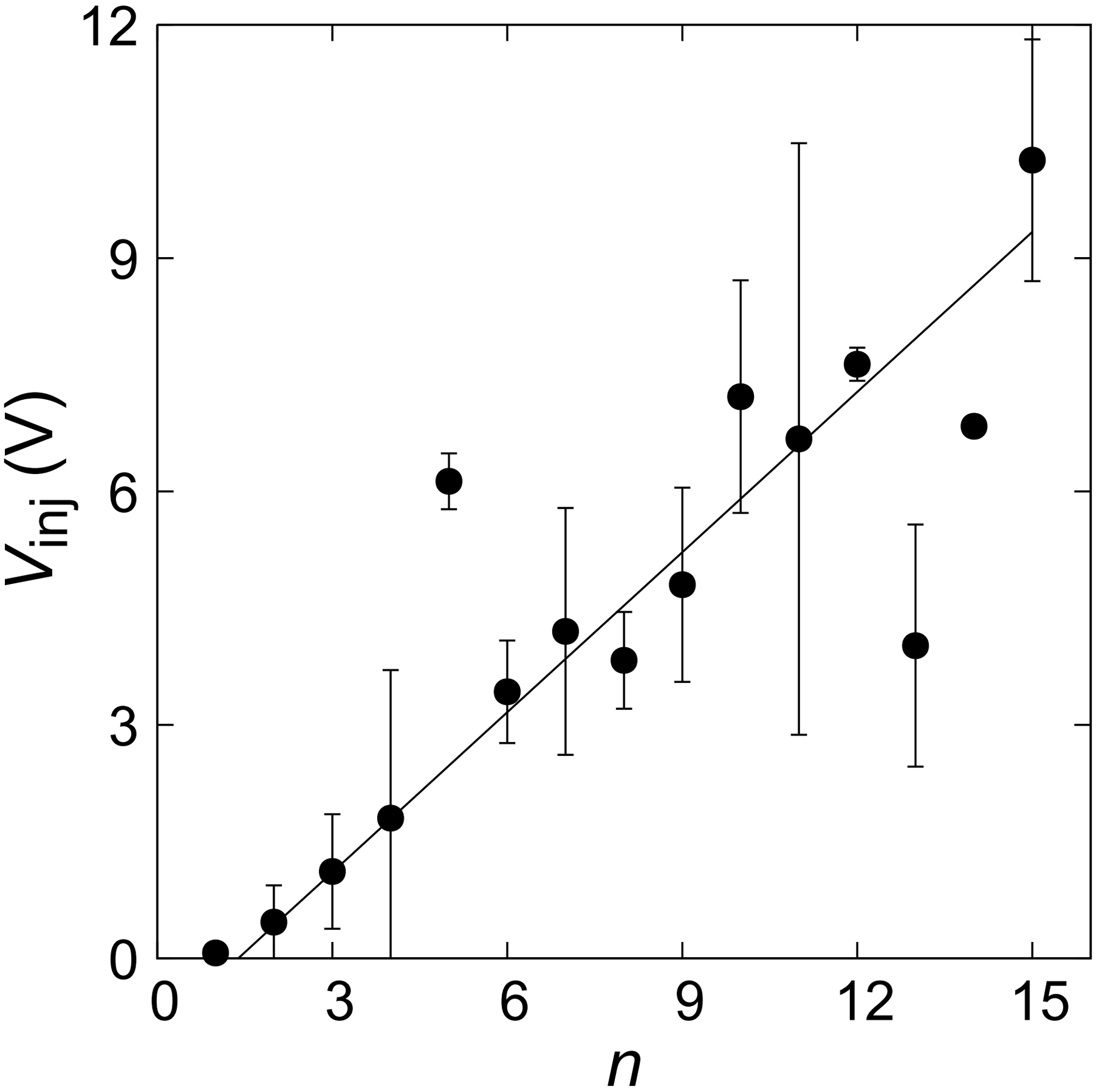
12
9
6
3
0
V_{inj} (V)
0
3
6
9
12
15
n

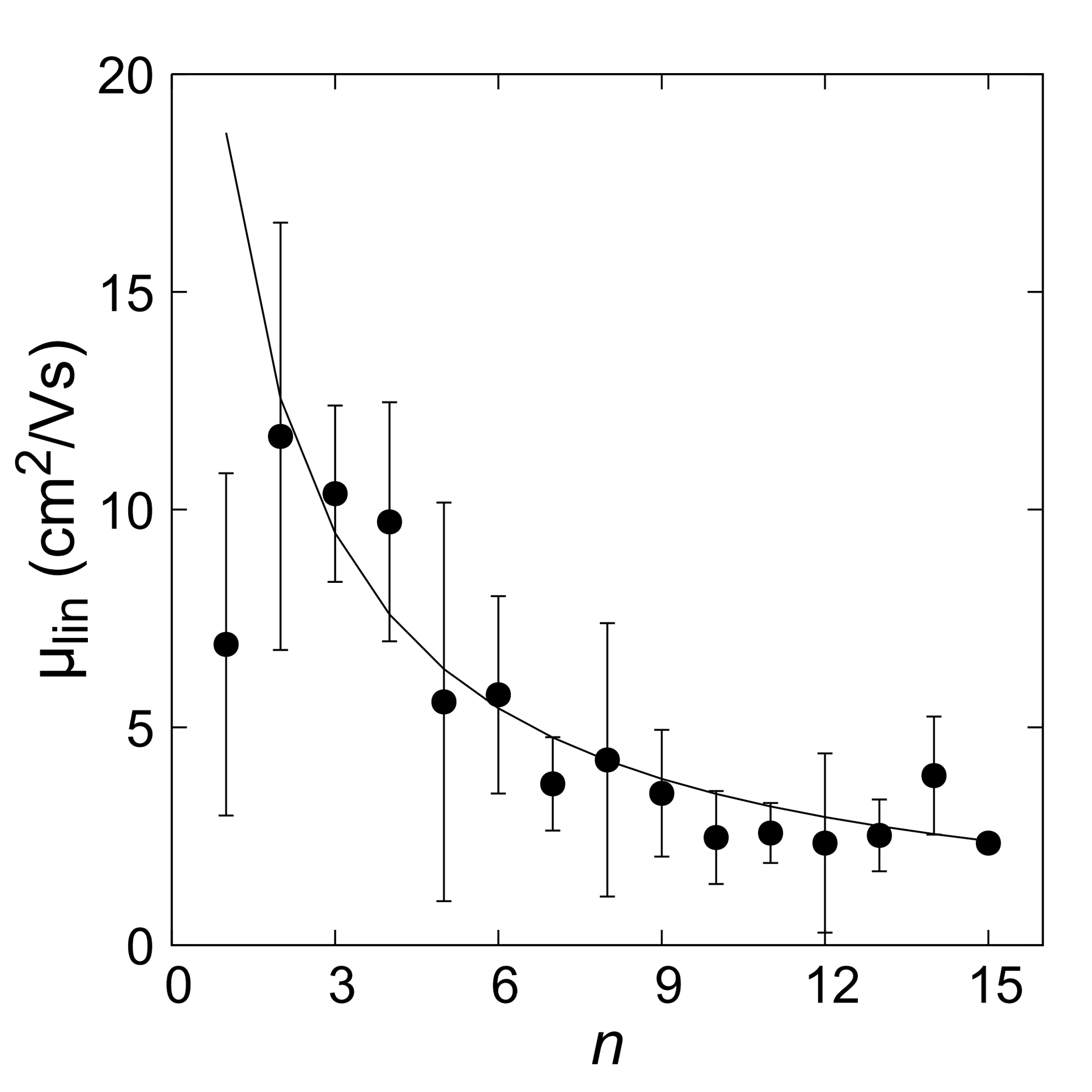
20
15
10
5
0
0
3
6
9
12
15
μ_{lin} (cm^2/Vs)
n

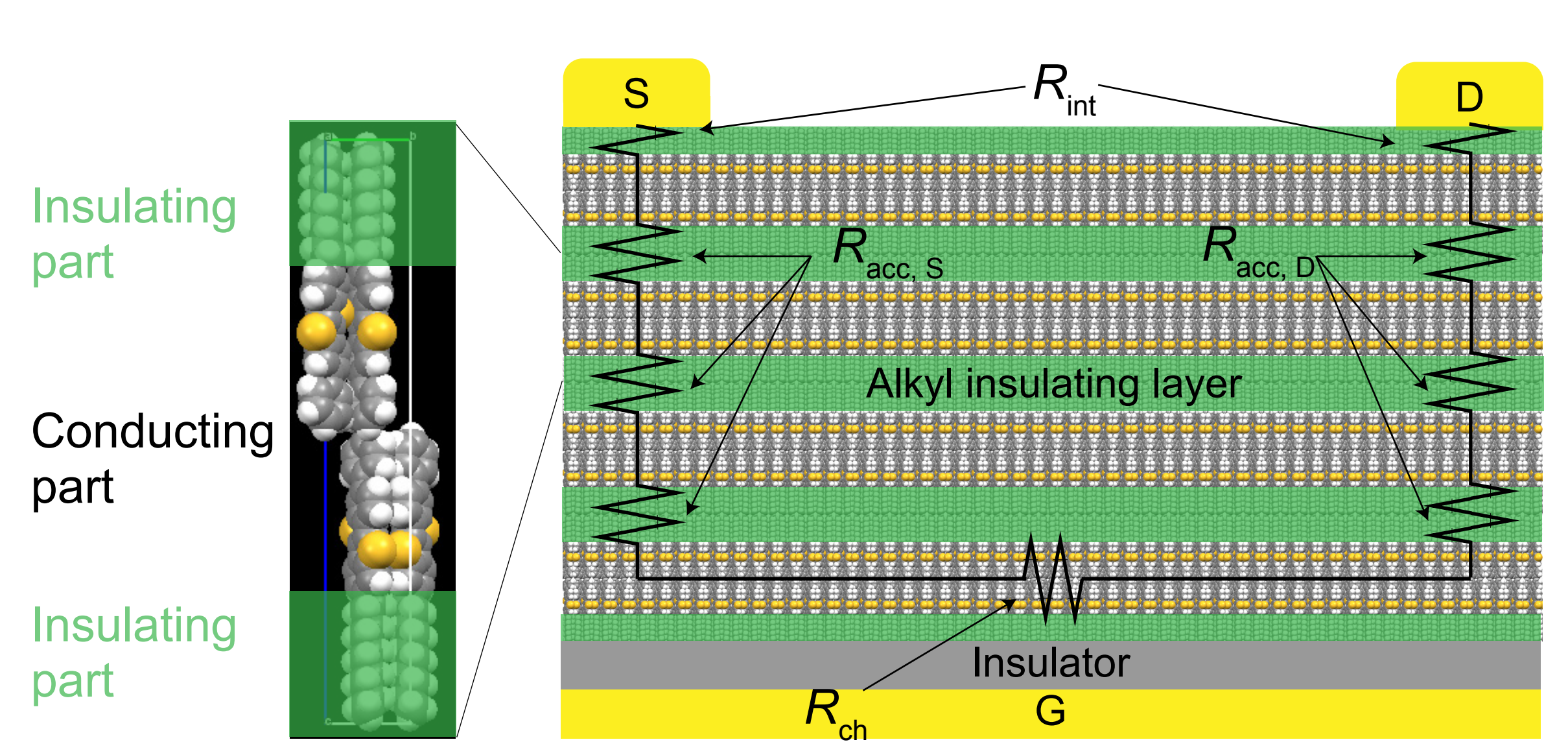
Insulating part
Conducting part
Insulating part
S
D
R_{int}
$R_{acc, S}$
$R_{acc, D}$
Alkyl insulating layer
Insulator
R_{ch}
G

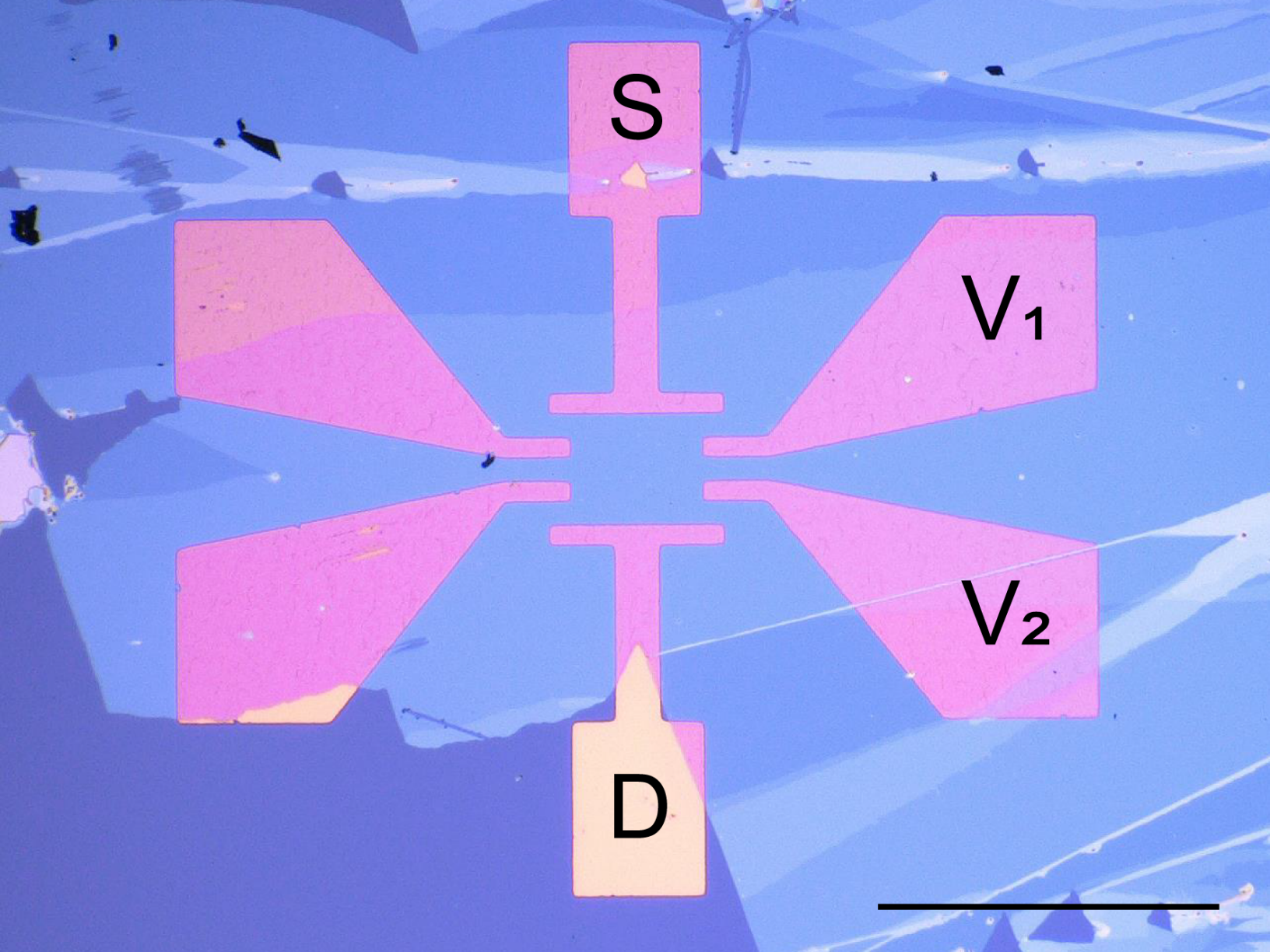
S
V1
V2
D

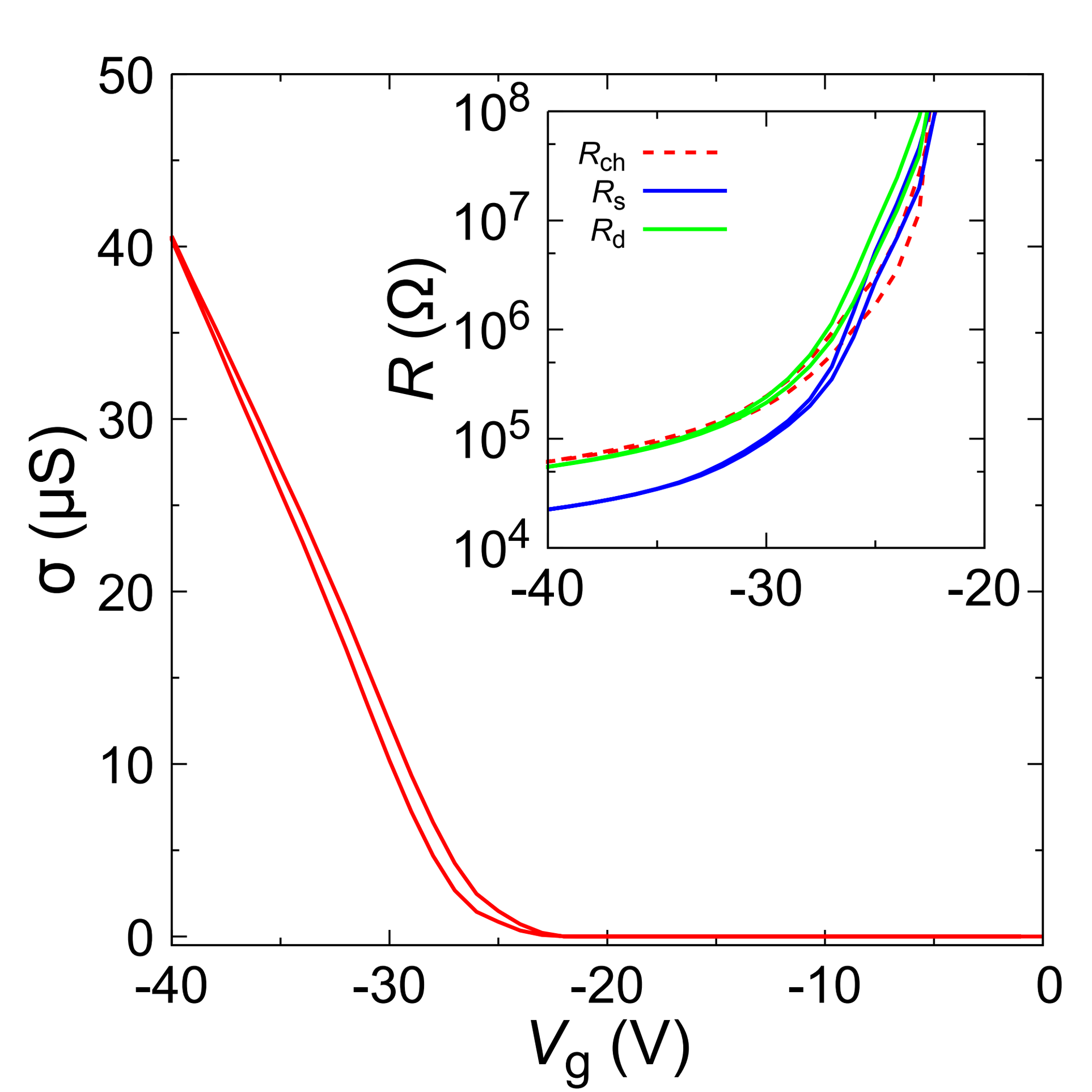
50
40
30
20
10
0
σ (μS)
-40
-30
-20
-10
0
V_g (V)
10^8
10^7
10^6
10^5
10^4
R (Ω)
R_{ch}
R_s
R_d
-40
-30
-20

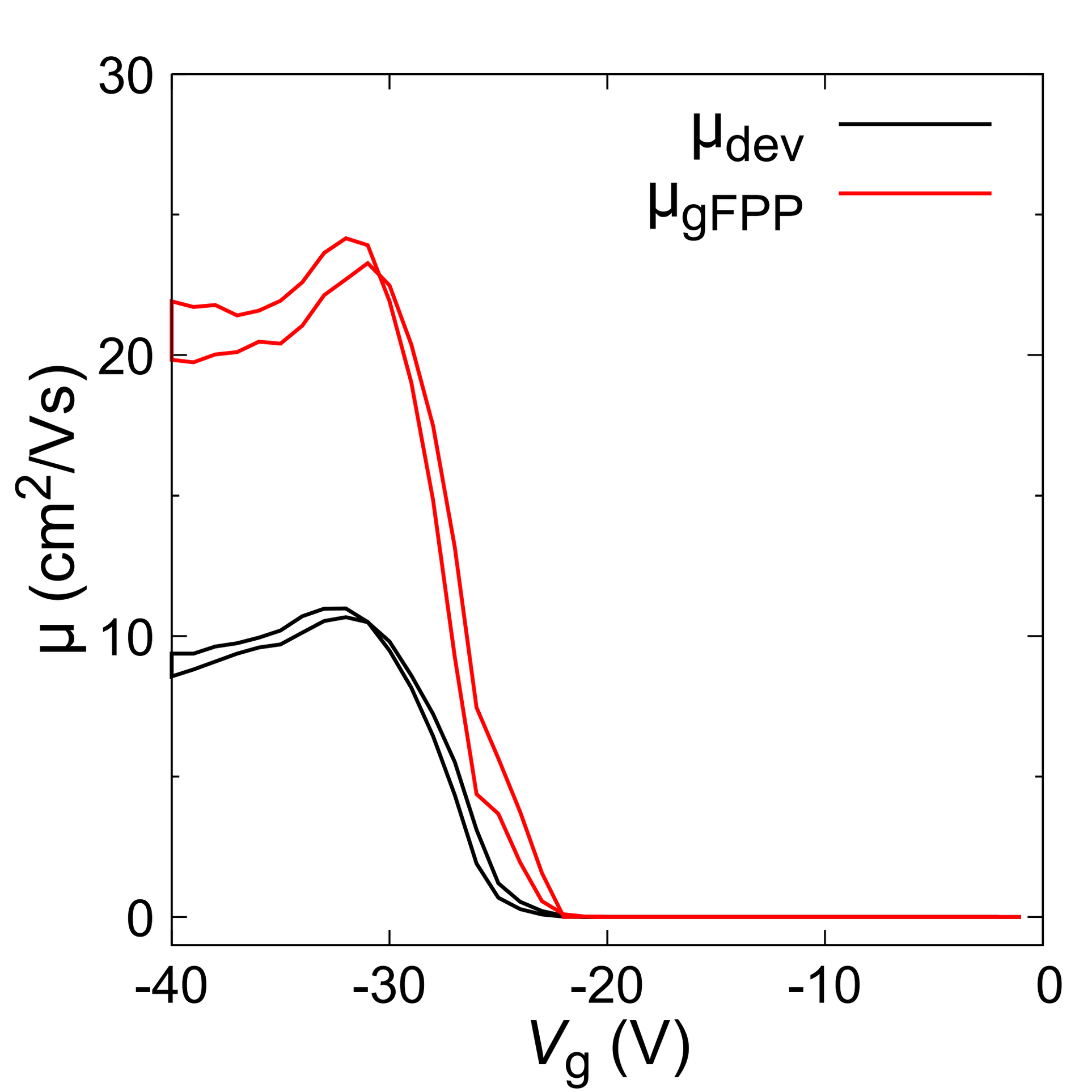
30
20
10
0
μ (cm²/Vs)
-40
-30
-20
-10
0
V_g (V)
μ_dev
μ_gFPP

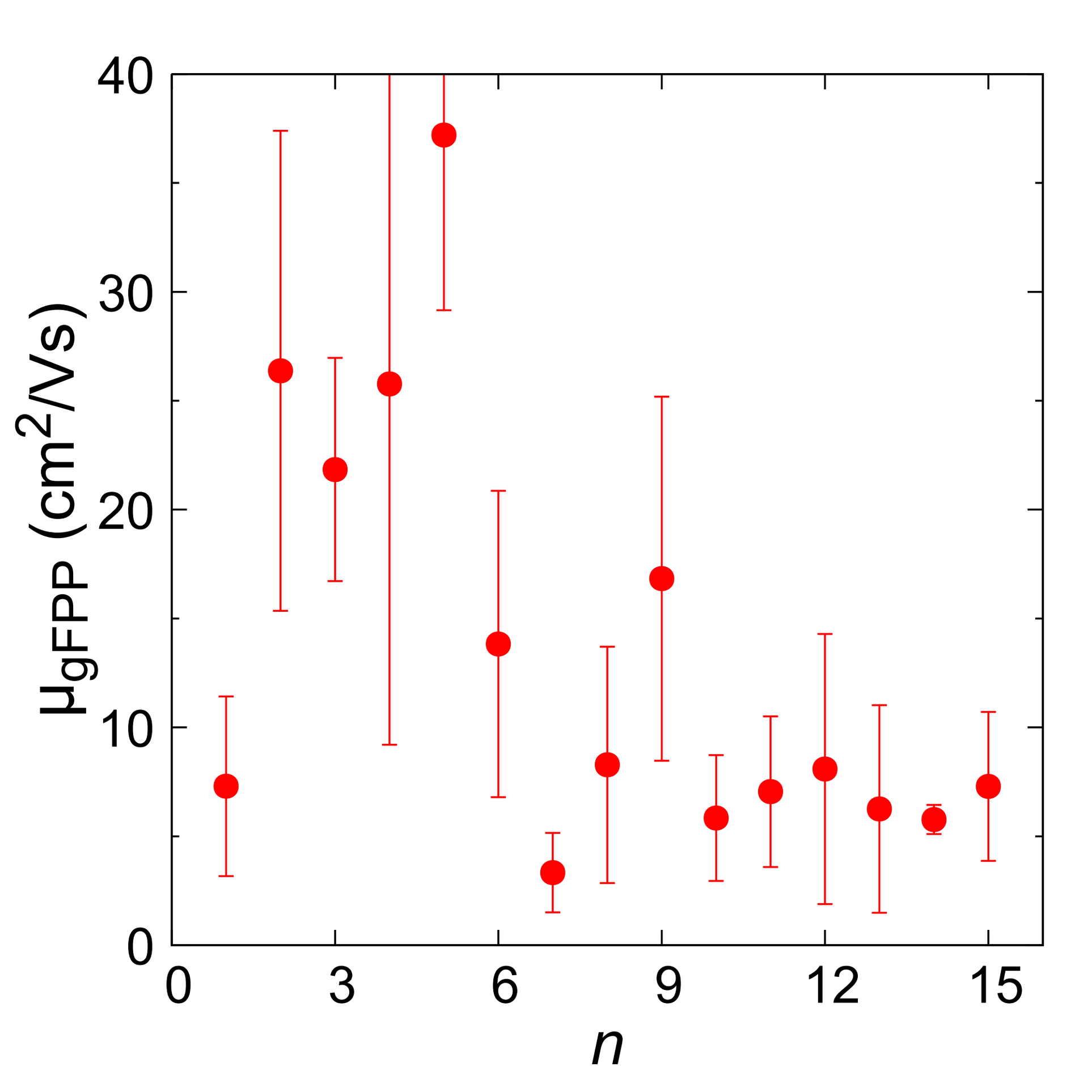
40
30
20
10
0
0
3
6
9
12
15
μ_{gFPP} (cm^2/Vs)
n

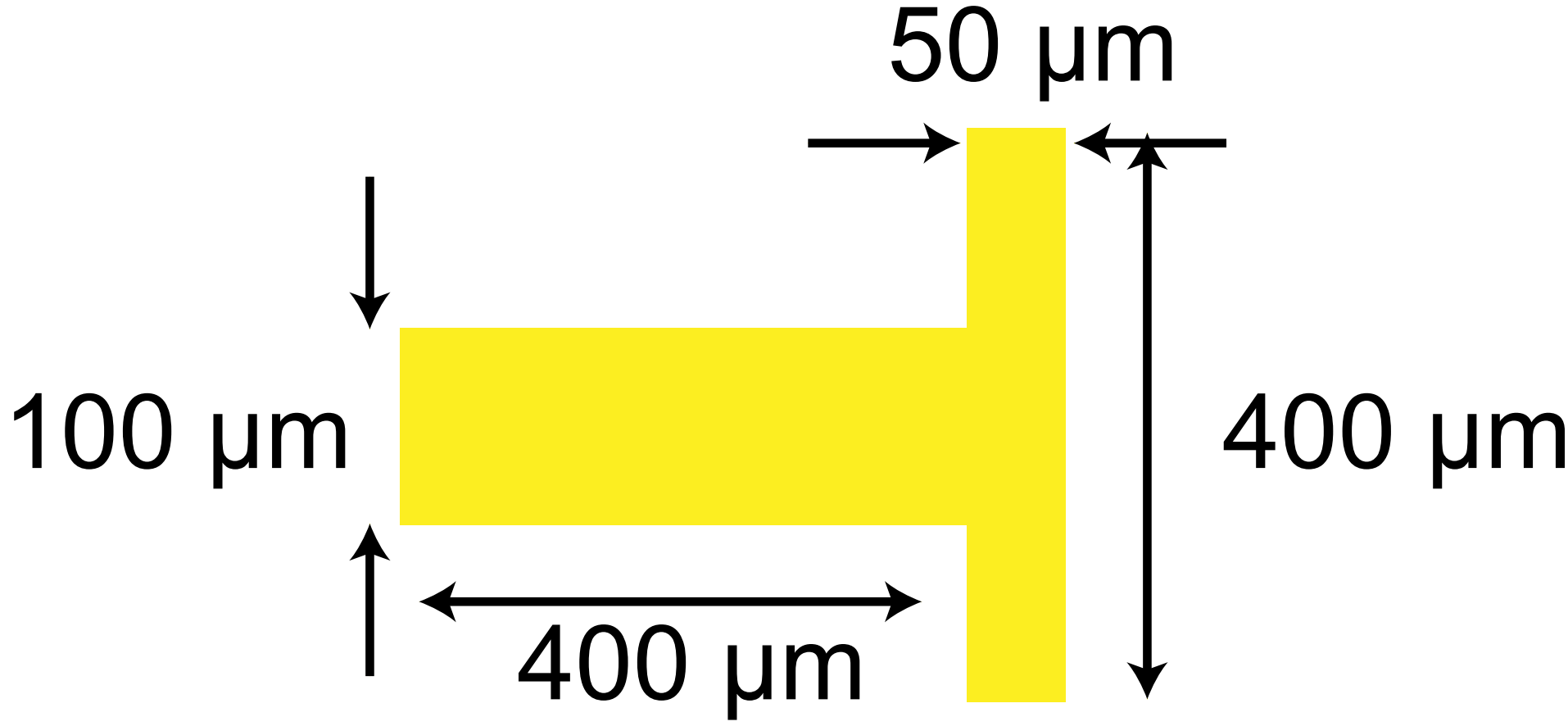
50 µm
100 µm
400 µm
400 µm

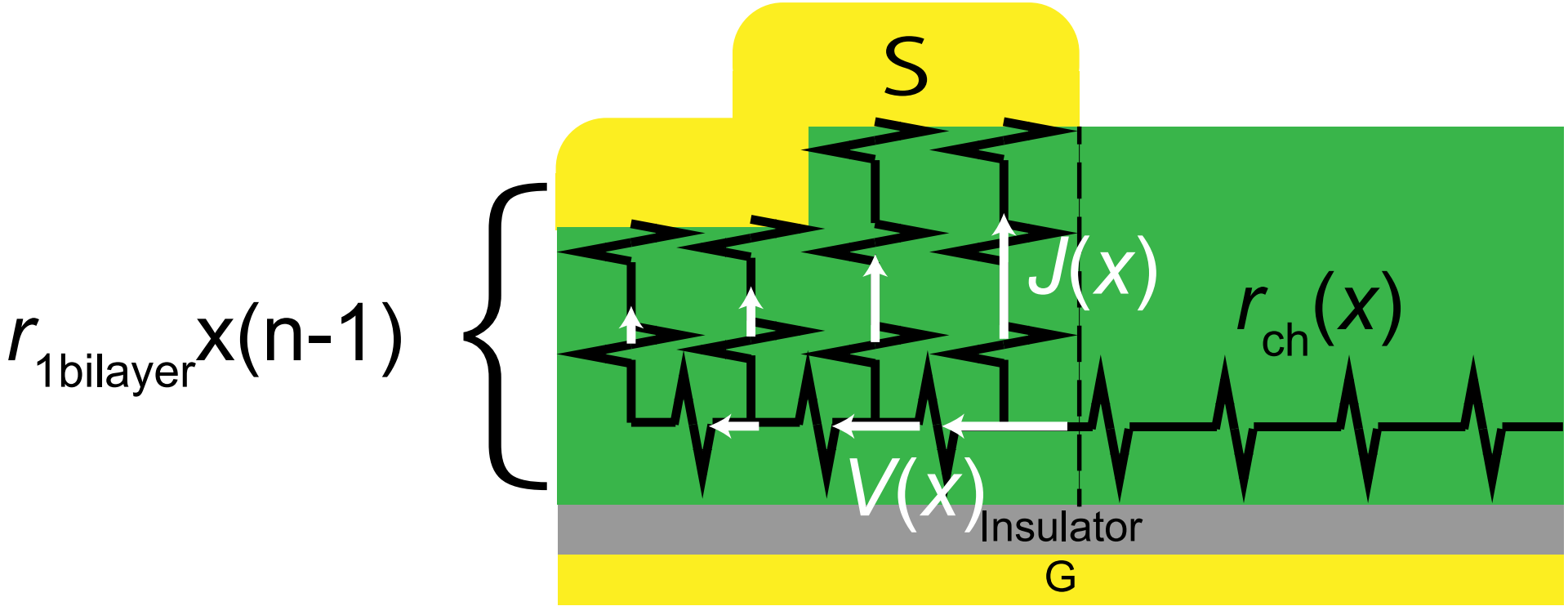
S
$r_{1bilayer}$x(n-1)
$J(x)$
$r_{ch}(x)$
$V(x)$
Insulator
G

μ^1_{dev} [cm^2/Vs]	θ	V_{inj} [V]
18.5	0.47	0.67(n-1)

	2 probe[a]	4 probe[a]	calculation[b]
R_{bilayer} [$10^4\Omega$]	1.2	0.97	0.34
$R_{\text{bilayer}}W$ [$10^2\Omega$cm]	4.7	3.9	1.4